

Air Force Institute of Technology

AFIT Scholar

---

Theses and Dissertations

Student Graduate Works

---

3-2020

## Mult-Spectral Imaging of Vegetation with a Diffractive Plenoptic Camera

Tristan R. Naranjo

Follow this and additional works at: <https://scholar.afit.edu/etd>



Part of the [Optics Commons](#), and the [Remote Sensing Commons](#)

---

### Recommended Citation

Naranjo, Tristan R., "Mult-Spectral Imaging of Vegetation with a Diffractive Plenoptic Camera" (2020). *Theses and Dissertations*. 4127.  
<https://scholar.afit.edu/etd/4127>

This Thesis is brought to you for free and open access by the Student Graduate Works at AFIT Scholar. It has been accepted for inclusion in Theses and Dissertations by an authorized administrator of AFIT Scholar. For more information, please contact [richard.mansfield@afit.edu](mailto:richard.mansfield@afit.edu).



**Multi-Spectral Imaging of Vegetation with a  
Diffractive Plenoptic Camera**

THESIS

Tristan R. Naranjo, 2d Lt, USAF  
AFIT-ENP-MS-20-M-108

**DEPARTMENT OF THE AIR FORCE  
AIR UNIVERSITY**

**AIR FORCE INSTITUTE OF TECHNOLOGY**

**Wright-Patterson Air Force Base, Ohio**

DISTRIBUTION STATEMENT A  
APPROVED FOR PUBLIC RELEASE; DISTRIBUTION UNLIMITED.

The views expressed in this document are those of the author and do not reflect the official policy or position of the United States Air Force, the United States Department of Defense or the United States Government. This material is declared a work of the U.S. Government and is not subject to copyright protection in the United States.

AFIT-ENP-MS-20-M-108

MULTI-SPECTRAL IMAGING OF VEGETATION WITH A  
DIFFRACTIVE PLENOPTIC CAMERA

THESIS

Presented to the Faculty  
Department of Engineering Physics  
Graduate School of Engineering and Management  
Air Force Institute of Technology  
Air University  
Air Education and Training Command  
in Partial Fulfillment of the Requirements for the  
Degree of Master of Science in Applied Physics

Tristan R. Naranjo, B.S. Physics

2d Lt, USAF

March 13, 2020

DISTRIBUTION STATEMENT A  
APPROVED FOR PUBLIC RELEASE; DISTRIBUTION UNLIMITED.

AFIT-ENP-MS-20-M-108

MULTI-SPECTRAL IMAGING OF VEGETATION WITH A  
DIFFRACTIVE PLENOPTIC CAMERA

THESIS

Tristan R. Naranjo, B.S. Physics  
2d Lt, USAF

Committee Membership:

Lt Col Anthony L. Franz  
Chair

Dr. Michael Marciniak  
Member

Dr. Michael Hawks  
Member

## Abstract

Snapshot multi-spectral sensors allow for object detection based on its spectrum for remote sensing applications in air or space. By making these types of sensors more compact and lightweight, it allows drones to dwell longer on targets or the reduction of transport costs for satellites. To address this need, I designed and built a diffractive plenoptic camera (DPC) which utilized a Fresnel zone plate and a light field camera in order to detect vegetation via a normalized difference vegetation index (NDVI). This thesis derives design equations by relating DPC system parameters to its expected performance and evaluates its multi-spectral performance.

The experimental results yielded a good agreement for spectral range and FOV with the design equations but was worse than the expected spectral resolution of 6.06 nm. In testing the spectral resolution of the DPC, it was found that near the design wavelength, the DPC had a spectral resolution of 25 nm. As the algorithm refocused further from design the spectral resolution broadened to 30 nm. In order to test multi-spectral performance, three scenes containing leaves in various states of health were captured by the DPC and an NDVI was calculated for each one. The DPC was able to identify vegetation in all scenes but at reduced NDVI values in comparison to the data measured by a spectrometer. Additionally, background noise contributed by the zeroth-order of diffraction and multiple wavelengths coming from the same spatial location was found to reduce the signal of vegetation. Optical aberrations were also found to create artifacts near the edges of the final refocused image. The future of this work includes using a different diffractive optic design to get a higher efficiency on the first order, deriving an aberrated sampling pattern, and using an intermediate image diffractive plenoptic camera to reduce the zeroth-order effects of the FZP.

## Acknowledgements

I'd like to thank my friends and family who've supported me through my physics endeavours. I'd also like to thank my research advisor who always asked thought provoking questions and guided me in the right direction.

Tristan R. Naranjo

# Table of Contents

	Page
Abstract .....	iv
Acknowledgements .....	v
List of Figures .....	vii
List of Tables .....	ix
I. Introduction .....	1
II. Background .....	5
2.1 Fresnel Zone Plate .....	5
2.2 Light Field Camera .....	9
2.3 Normalized Difference Vegetation Index .....	16
III. Theory .....	20
3.1 Design Equations .....	20
3.2 Multi-Spectral Imaging .....	29
IV. Experiment .....	33
4.1 DPC Construction .....	33
4.2 Test Profiles .....	41
V. Results and Analysis .....	50
5.1 Spectral Resolution Performance .....	50
5.2 NDVI & Multi-Spectral Performance .....	56
VI. Conclusion .....	65
6.1 Contributions .....	65
6.2 Future Work .....	66
Bibliography .....	69

## List of Figures

Figure		Page
1	Push-broom scanning on a FPA .....	2
2	Planar wavefront impinging upon a Fresnel zone plate .....	5
3	Spectral resolution of a FZP .....	8
4	LFC setup .....	11
5	LFC ray-space diagram .....	12
6	4-D Coordinate system on FPA .....	14
7	Shift-and-add refocusing algorithm .....	16
8	Visible-NIR reflectance spectra of vegetation .....	17
9	Effect of multiple leaf layers on reflectance .....	18
10	DPC setup .....	21
11	DPC ray-space diagram .....	22
12	Spatial-angular relation ray diagram .....	25
13	DPC spectral resolution .....	27
14	Zeroth-order effect .....	31
15	FPA spectral cross-talk .....	32
16	MLA and FPA experimental setup .....	35
17	Experimental setup of the laser .....	36
18	Lenslet center detection .....	37
19	MLA re-sampling .....	38
20	Lenslet center detection verification .....	40
21	Spectral resolution calculation .....	42
22	Reflectance measurement setup .....	44

Figure	Page
23	DPC vegetation scenes ..... 48
24	DPC source scenes ..... 49
25	Integrated PSF values ..... 51
26	Peak irradiance refocused images ..... 53
27	Spectral resolution of the DPC ..... 54
28	Spectrometer reflectance measurements ..... 57
29	DPC refocused Scenes ..... 58
30	DPC reflectance measurements ..... 59
31	DPC NDVI measurements ..... 61
32	Abberated sub-aperture view ..... 62
33	Lenslet and sub-aperture image formation ..... 63
34	Reduced sub-aperture NDVI ..... 64
35	Aberrated sub-aperture NDVI ..... 64
36	Intermediate image DPC ..... 67

## List of Tables

Table		Page
1	Fresnel zone plate design parameters .....	34
2	Micro lens array parameters .....	34
3	Focal plane array parameters .....	34
4	DPC parameters .....	41
5	FWHM of integrated PSF values .....	51

# MULTI-SPECTRAL IMAGING OF VEGETATION WITH A DIFFRACTIVE PLENOPTIC CAMERA

## I. Introduction

Multi-spectral imagers allow for spatial discrimination within a scene for a particular band of wavelengths. Setups commonly involve a band-pass filter that is placed either in front of the entire sensor to maximize spatial sampling [1] or an array of band-pass filters, which allows for imaging multiple spectral bands on one sensor at reduced spatial sampling [2]. Typical uses for multi-spectral imagery in remote sensing are identifying objects based on their spectral structure. The normalized difference vegetation index is one object detection algorithm which determines if vegetation is in a scene based on the reflectance in the near-infrared and red band [3].

There are other methods to capture multi-spectral imagery such as hyperspectral cameras. These types of cameras allow for the capture of many continuous spectral bands by incorporating a dispersive element within the optical system or creating an interferogram [4]. The downside of hyperspectral cameras is that many of them require time to collect an entire scene. One method frequently used to capture a hyperspectral data cube is called push-broom scanning, which is displayed in Figure 1. The incident wavefront is focused down to a slit to allow one column's worth of spatial data and sent through a dispersive optic to separate its spectrum along the row. In order to build a complete data cube, multiple frames are taken of the scene to gather the other spatial direction. There has been other research on snapshot hyperspectral cameras such as the computed-tomography imaging spectrometer [5] or the Hyperpixel array camera [6] but both require a large amount of spatial sampling.

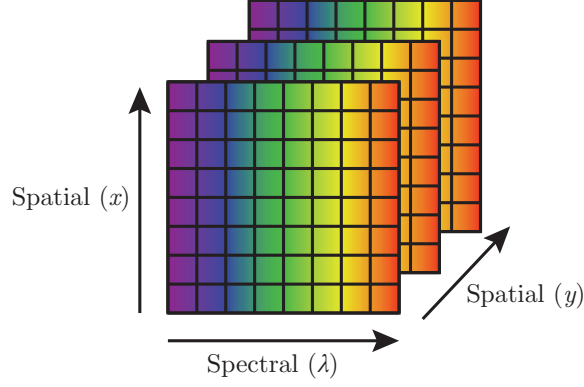


**Figure 1. Push-broom scanning method to collect hyperspectral data. Each row contains the spectral information of one pixel. Multiple frames are taken to build a complete data cube in the  $y$  direction.**

The diffractive plenoptic camera (DPC) introduces a new way to capture multi-spectral imagery by using computational imaging. This idea of combining a plenoptic camera and an axial dispersion lens was introduced by Zhou [7] and further refined by Hallada by using a Fresnel zone plate as the optic [8]. The plenoptic camera is unique from conventional imagers as it places a microlens array at the focus of the imaging optic and places the focal plane array detector at the focus of the microlens array. By adding the microlens array, it enables the plenoptic camera to determine the angle the ray of light came from and where the ray originated from the object plane. Taking advantage of this fact, Ng in his dissertation used it to create his light field camera, which allows for digital refocusing after the photo has been taken [9]. The process is done by computationally shifting the values of the pixels to where the ray of light should have intercepted the sensor if it were at that focal plane. Hallada in his thesis took a step further and replaced the primary optic with a Fresnel zone plate, which is known for its severe axial chromatic aberration [10]. This system, formally known as the Fresnel zone light field spectral imager, and more recently called the diffractive plenoptic camera, places the object out at infinity or a constant depth from the camera. The incident light is diffracted to different focal lengths based

on its wavelength instead of its depth. By using a computational method similar to that of Ng, this allows the image to be “refocused” to different spectral bands of the scene, allowing it to keep its spatial information as well.

The advantage of the DPC is that it uses diffractive optics, which are traditionally lighter and offer other unique benefits than their refractive counterpart. One example is USAFA’s FalconSat 7, which utilizes a deployable photon sieve membrane to create a sizeable primary optic for a cube satellite package [11]. The downside of the FalconSat 7 is that it can only image one narrow spectral band that severely limits the light gathering ability of the system. By using a DPC on a cube satellite like this one, it would expand the number of spectral bands imaged and would not be limited to only bright sources. Additionally, if the number of spectral bands required is low, which is the case for the normalized difference vegetation index, there is no need for the fine spectral sampling of a hyperspectral camera, which will be more costly and cumbersome.

Previous work done on the DPC looked into some of the critical components that make up the system. Diaz looked at the spatial resolution and contrast of the DPC with another similar system called the intermediate image diffractive plenoptic camera (IIDPC) [12]. The IIDPC is based on the focused plenoptic camera, which alters the microlens array location to gain a higher spatial sampling than the light field camera [13]. The difference is that the IIDPC replaces the primary optic with a diffractive one. Shepard looked at a simulation of how different refocusing algorithms like Gaussian smoothing, super-resolution, and deconvolution affected quantities like spatial resolution, spectral resolution, and spectral range [14].

This thesis will give the first experimental demonstration of the DPC to capture multi-spectral scenes. To begin, background will be provided on the Fresnel zone plate and light field camera to explain how the DPC works. Next, the spectral

structure of vegetation will be explained and the normalized difference vegetation index will be defined. Afterward, design equations will be derived to relate system parameters to their estimated multi-spectral performance. Background noise sources, such as spectral cross-talk, will be addressed due to the poly-chromatic nature of scenes. Next, steps taken to calibrate the DPC and verification of the algorithm will be shown. The first experimental setup looked at how well the refocusing algorithm is able to spectrally resolve two wavelengths in the absence of spectral background noise. Finally, the second experiment captures the spectra of three different leaves in various states of health and calculates a normalized difference vegetation index.

## II. Background

This chapter will provide necessary information about the components of the diffractive plenoptic camera and the spectra of vegetation. The first two sections discuss the Fresnel zone plate and Ng's light field camera with an emphasis on equations that govern its properties. The last section describes the spectral structure of vegetation and how the normalized difference vegetation index quantifies the scene to determine if plants are present. Fundamental equations that govern the diffractive plenoptic camera are reserved for the next chapter.

### 2.1 Fresnel Zone Plate

The primary optic of the DPC consists of a circular binary Fresnel zone plate (FZP), which exploits the diffractive optic's axial chromatic aberration. For purposes of this thesis, all wavefronts are treated as if they are coming from infinity. To begin, Figure 2 displays a monochromatic planar wave incident upon a section of a FZP where  $w_n$  is the width of zone  $n$ ,  $r_n$  is the radius to the  $n^{\text{th}}$  zone,  $l_n$  is the path length from  $r_n$  to point P, and  $f$  is the focal length of the FZP.

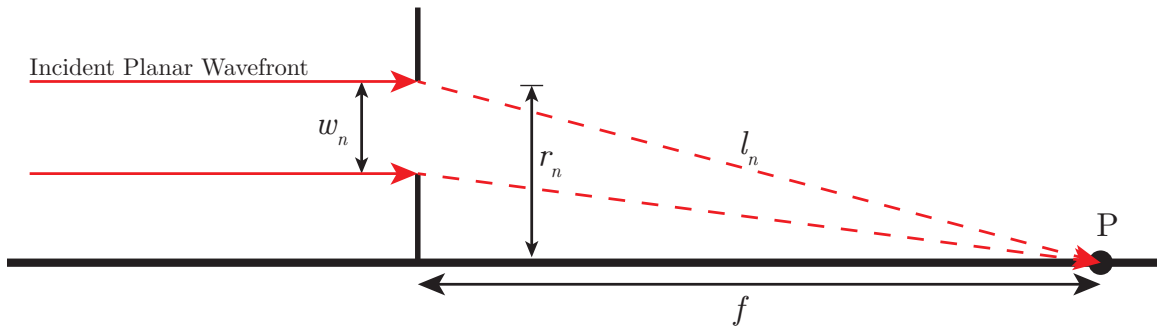


Figure 2. A 1-D representation of how incoming planar waves are diffracted to the focus in a Fresnel zone plate. Each zone  $n$ , are placed in a way such that the path length  $l_n$  is  $\lambda/2$  longer than the previous path length to map out areas of the wavefront that have a positive or negative phase. Blocking all the positive or negative phase fronts will result in constructive interference at the focal length, point P.

In order to achieve focus at point P, the diffracted light needs to constructively interfere. This means the zones need to block parts of the wavefront that have a  $\pi$  phase difference. The condition is achieved when the path length is  $\lambda/2$  greater than the previous path length as described by

$$l_n - f_0 = \frac{n\lambda_0}{2} \quad (1)$$

where  $f_0$  is the designed focal length of the zone plate and  $\lambda_0$  is the wavelength designed for that focal length.  $l_n$  can be placed in terms of  $r_n$  and  $f_0$  using the Pythagorean theorem. Solving for the radius leads to

$$r_n^2 = n\lambda_0 f_0 + \left(\frac{n\lambda_0}{2}\right)^2 \quad (2)$$

Typically, the  $(n\lambda_0/2)^2$  term is much smaller than the previous term for optical frequencies[15]. This approximation gives the radius of each zone to be

$$r_n^2 \approx n\lambda_0 f_0 \quad (3)$$

Generally, the design of the FZP will have a set diameter and focus for the design wavelength to meet the f-number matching condition described in the next section about the light field camera. For wavelengths other design,  $r_n$  remains constant but the focal length changes as a result of the path length condition in equation 3. The resulting focal length for wavelengths other than design is

$$f_\lambda = \frac{f_0 \lambda_0}{\lambda} \quad (4)$$

where  $\lambda$  is the incident wavelength and  $f_\lambda$  is the focal length for the incident wavelength.

To determine the spatial resolution and the size that an FZP can be manufactured to, the width of the smallest zone is calculated. Attwood derives this by taking equation 3, subtracting the last zone by the previous one and making the approximation that the width of the smallest zone is much less than the radius of the FZP for a large  $N$ , the last zone [16]. The width of the last zone,  $w_N$  becomes

$$w_N = \frac{\lambda_0 f_0}{2r_N} \quad (5)$$

where  $r_N$  is the radius of the FZP. Equation 5 is approximately equal to the spatial resolution of the FZP using the Rayleigh criterion [17]. Additionally, manufacturers can only produce features down to a limit, which in a binary FZP, the smallest feature is  $w_N$ . The last zone's width will then limit the radius of the FZP.

For parameters such as the spectral resolution and the maximum field of view (FOV) of a FZP, the total number of zones needs to be calculated. By taking equation 3 and solving for  $n$  at  $r_N$ , the total number of zones becomes

$$N = \frac{r_N^2}{\lambda_0 f_0} \quad (6)$$

where  $N$  is the total number of zones. To find the spectral resolution of the FZP using the Rayleigh criterion, the irradiance as a function of distance from the FZP needs to be known. Sussman derives this by taking a geometric series of an exponential that results from taking an integral over the transparent zones of the FZP [18]. The resulting equation with variables to fit this thesis is

$$E(0, 0, z) = \frac{\sqrt{f_0 \lambda_0} [1 - \cos(N \frac{\pi f \lambda}{z})]}{(\frac{\pi f \lambda}{z})^2 [1 + \cos(\frac{\pi f \lambda}{z})]} \quad (7)$$

where  $z$  is the distance from the FZP. This equation is the ultimate spectral resolution

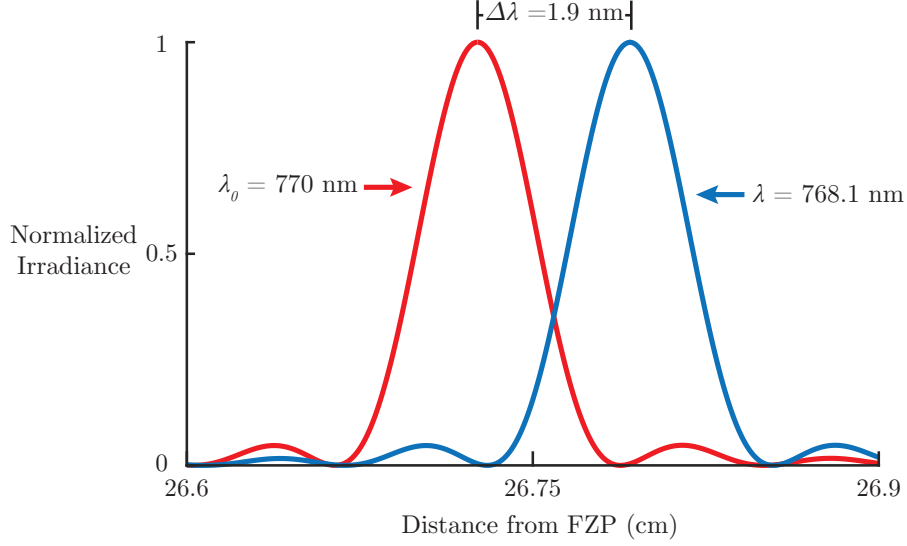


**Figure 3.** Spectral resolution of a FZP which has the following parameters:  $\lambda_0 = 770$  nm,  $f_0 = 267.26$  mm,  $r_n = 13.34$  mm, and  $N = 864$  rings. Using the Rayleigh criterion, the second incident wavelength of equal irradiance was placed at the first minimum of the design wavelength, leading to a spectral resolution of  $\Delta\lambda = 1.9$  nm.

the DPC can achieve; however the DPC's resolution will also be affected by other factors of the light field camera. An example of the maximum spectral resolution of the FZP in this experiment is given in Figure 3.

Unlike a regular refractive optic, the FZP will have a limit on the maximum FOV it can achieve before it no longer produces well-defined edges due to errors in the optical path distance. According to Myers the maximum off-axis angle to maintain good focus [19] is

$$\left| \pm (f_0 N \lambda)^{1/2} \left( \frac{N \lambda}{2 f_0} \right) \sin(\epsilon) - \frac{N}{2} \lambda \sin^2(\epsilon) \right| < \frac{1}{4} \lambda \quad (8)$$

where  $\epsilon$  is the half angle from the optical axis. For the FZP used in this experiment the FOV of good focus was approximately  $7^\circ$ .

The last parameter to calculate for the FZP are the diffraction efficiencies for each order. According to equation 7, there are multiple irradiance peaks for a given

wavelength behind the FZP. In practice, the use of the first positive order of diffraction is considered the primary focal length used in equation 4. The additional focal lengths occur at distances  $f_0/m$  for odd integers of  $\pm m$ , where  $m$  is the diffraction order. Theoretically, even integers of  $\pm m$  do not occur because the number half-period zones contributing to the focus will cancel each other out, but in practice they are seen due to manufacturing errors. In contrast to the odd integers, there will always be one more half-period zone that will not be canceled out [20]. For  $m = 0$ , this is considered the zeroth diffraction order which does not interact with the FZP and passes straight through.

The diffraction efficiency is a measurement of how efficient the diffractive optic can focus the incident light to its different orders. For a binary FZP, 50% of the light is absorbed by the plate itself while the remaining amount is placed into the following diffraction orders

$$\eta_m = \begin{cases} \frac{1}{4} & m = 0 \\ \frac{1}{m^2\pi^2} & m = \text{odd} \\ 0 & m = \text{even} \end{cases} \quad (9)$$

where  $\eta_m$  is the diffraction efficiency of order  $m$  [16]. Most notably the zeroth-order contains 25% of the incident energy while the first-order contains about 10% of the incident energy. In practice, the diffraction efficiencies will slightly differ due to errors in the manufacturing process and the zone sizes not precisely matching the theoretical values [21].

## 2.2 Light Field Camera

The idea leading to the light field camera began with the plenoptic function, which describes the irradiance, chromaticity, position, and time of a ray of light to an observer [22]. Using the idea of the plenoptic function, Adelson and Wang developed

the plenoptic camera, which aimed to derive passive depth measurements with only one camera instead of using a binocular stereo system [23]. The plenoptic camera worked well comparatively if a small parallax was acceptable. The next evolution of the plenoptic camera pioneered by Ng was the light field camera (LFC), which allowed a photograph to be digitally refocused to different depths after it had been taken [24]. The light field is a re-parameterization of the plenoptic function in which it is only concerned with the light inside the camera body from the object plane from which it came in that instant of time. The resulting functional form of the light field that will be used throughout this thesis is  $L(u, v, x, y)$ , where  $(u, v)$  is the intersection of the ray of light and the aperture. These will be called the angular coordinates.  $(x, y)$  is the intersection of the same ray of light with the microlens array (MLA) and will be called the spatial coordinates.

To begin to understand how the LFC works, Figure 4 demonstrates how rays propagate through the system along with variable designations. An object is considered in-focused when it is imaged onto the MLA plane like the point source in the figure. The rays from the point source will then converge onto one lenslet. From here, the rays will be refracted by the lenslet onto the focal plane array (FPA), which is placed at a lenslet's focal length,  $f_\mu$ , away. Notice that each pixel behind the lenslet corresponds to a patch of an area on the primary optic. In the case of Figure 4, there are five pixels behind each lenslet, which corresponds to the same number of sections into which the primary optic is divided. The width of each section is the angular sampling  $\Delta u$ , while the width of each lenslet is the spatial sampling  $\Delta x$ . Here it is shown that the LFC trades some of its spatial sampling for angular sampling in order to refocus images. The geometry of a lenslet image illuminating only the sensor behind it is satisfied when the image-side f-number of both the primary optic and MLA are the same. If the two components are not f-number matched, then the resulting lenslet

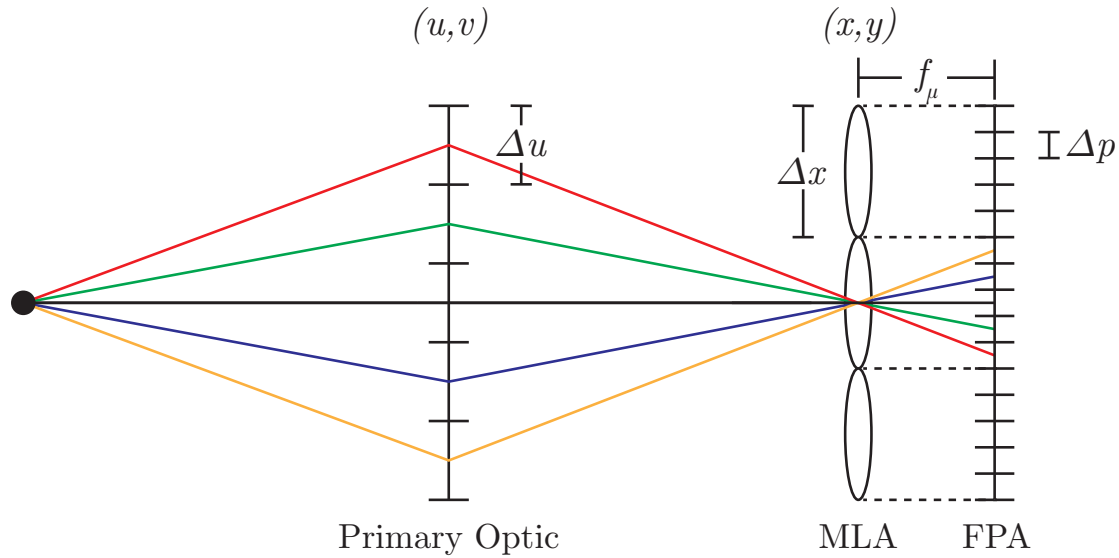
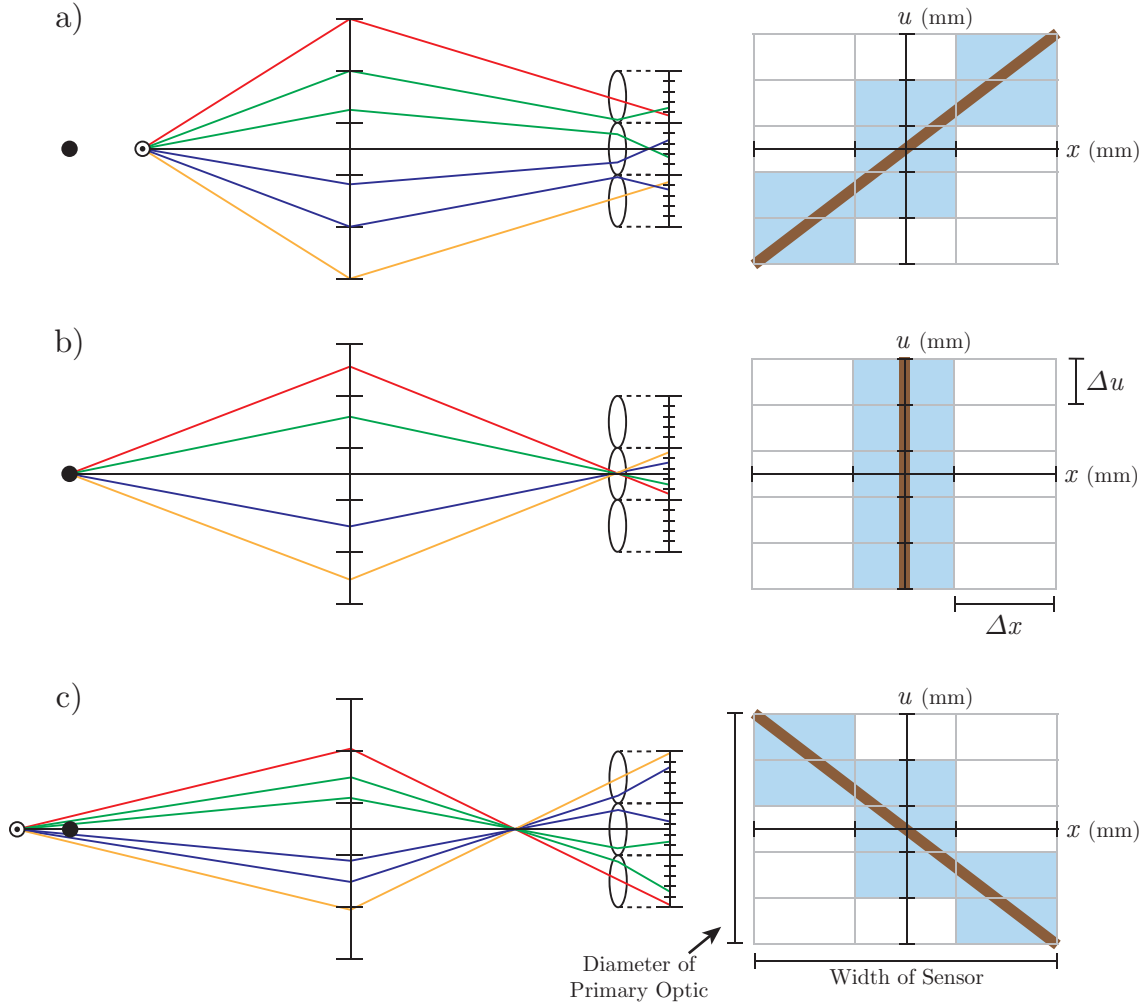


Figure 4. For point sources at the in-focus plane of the LFC, the light fully illuminates the primary optic and focuses down to one lenslet. The rays are refracted by the MLA onto the FPA placed at a lenslet focal length away. Each pixel corresponds to a section outlined on the primary optic. This geometry only holds when the primary optic and the MLA are image-side f-number matched. Each lenslet is a spatial sample of size  $\Delta x$ , and each section on the primary optic is an angular sample of size  $\Delta u$ , which is related to a pixel of size  $\Delta p$ .

images will either bleed into other lenslet images, or the images will be smaller than the area behind it. An excellent visual description is shown in Ng's dissertation on page 35, Figure 3.7 [25].

As the point source moves off of the in-focus plane, the rays will no longer converge onto one lenslet. To help keep track of where rays deposit their energy to which pixel, it is essential to introduce the ray-space diagram displayed in Figure 5. In a), the left figure shows a point source that is closer than the in-focus plane. As a result, the rays will focus past the MLA and will illuminate multiple microlenses. The corresponding ray-space diagram is displayed to the right of the image. The positive values for  $x$  and  $u$  are associated with intersections above the primary optic's optical axis, and negative values are intersections below it. Following the red ray in the LFC, it gets refracted by the topmost portion of the primary optic, which leads to the highest



**Figure 5. The effect of objects off the in-focus plane and its graphical representation. Each color represents a ray coming from a specific section of the primary optic and will end at the same relative pixel position behind each lenslet. Positive values for both the angular and spatial coordinates,  $u$  and  $x$ , will be above the optic axis of the primary optic, while negative values are below it. a) For objects closer than the in-focus plane, the rays will still be converging as they impinge on the MLA and illuminate multiple lenslets. The resulting ray space diagram will have a positive slope. Each teal box is a discrete data point from the FPA, and the thick brown line is the continuous data representation. b) objects at the in-focus plane illuminate only one lenslet and results in a vertical line. c) objects further than the in-focus plane, focus closer than the MLA and results in rays diverging, illuminating multiple lenslets. The ray-space diagram results in a negative slope.**

value of  $u$  and intersects with the topmost lenslet, which also leads to the highest value of  $x$ . The corresponding box is illuminated blue because the sampling is discrete on the sensor. The remaining boxes are illuminated from the corresponding rays that

make the appropriate intersections with both of these planes. If the system were not discrete, the resulting plot would show a positive slope on the ray-space diagram, indicated by the thick brown line. The slope is indicative of objects that are closer than the in-focus plane. As the object moves back, the ray-space diagram becomes a vertical line for objects at the in-focus plane as displayed in b) and has a negative slope for objects that are further than the in-focus plane displayed in c). Lastly, it is essential to note that each ray corresponds to the same relative pixel behind each lenslet image regardless of the object distance. As an example, the red ray will always refract to the bottom pixel in the lenslet image in all three object depths.

The next important aspect of the LFC is asking how far an object can be from the in-focus plane before the LFC can no longer refocus to that depth. This range of depths is considered the “Perfect Digital Refocusing” range, where the algorithm can refocus to before the spatial sampling is not equal to the original sampling. The refocusing range comes from Ng’s dissertation in which he takes a band-limited light field and uses his Fourier Slice Photograph Theorem to derive [25]

$$|F' - F| \leq \frac{\Delta x N_u F'}{W_u} \quad (10)$$

where  $F$  is the distance from the primary optic to the MLA,  $F'$  is the image distance of the object,  $W_u$  is the width of the primary optic in  $u$  direction, and  $N_u$  is the number of angular samples in the  $u$  direction. To place equation 10 in terms of system parameters, other relations are required. The number of spatial samples are  $N_x = W_x/\Delta x$  and the number of angular samples are  $N_u = W_u/\Delta u$ , where  $W_x$  is the width of the FPA in the  $x$  direction. The number of angular samples is also equal to the number of pixels behind each lenslet:  $N_u = \Delta x/\Delta p$ , where  $\Delta p$  is the width of the pixel in the  $x$  direction. By making the appropriate substitutions, the “Perfect Digital Refocusing” range in terms of system parameters becomes equation 11 [25].

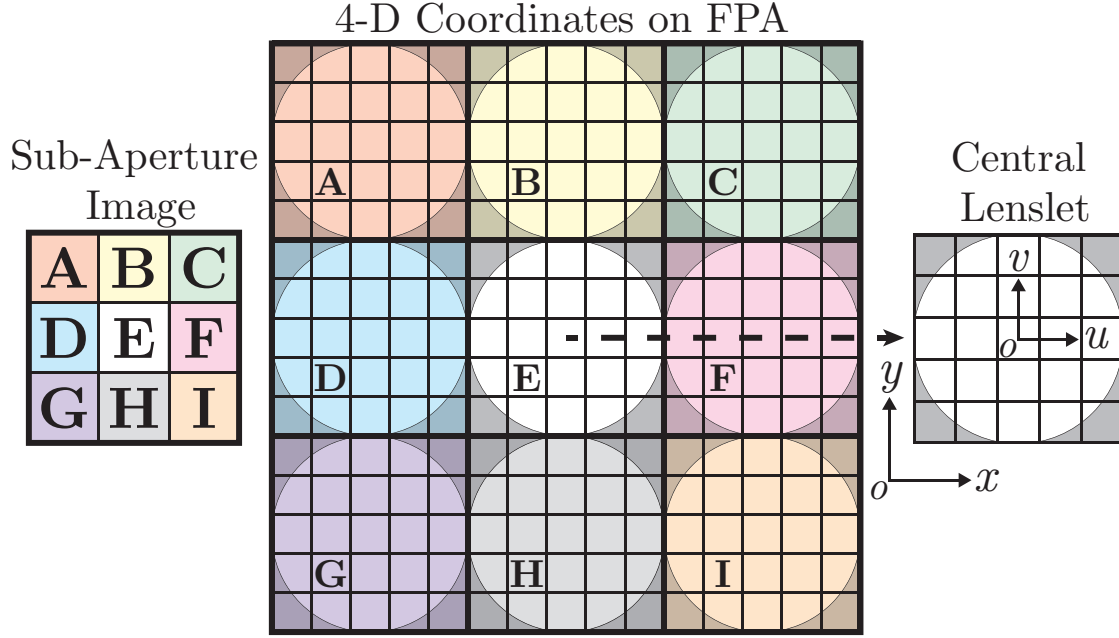


Figure 6. The grid in the middle represents how the FPA is divided into a 4-D coordinate system. Each colored square is an area behind a single lenslet. The circle under colored square is an image of the aperture of the primary optic. For the spatial coordinates,  $(x, y)$ , the origin starts at the center of the FPA. The range the spatial coordinates can take is the width of the sensor in their respective direction. The image to the right of the FPA displays the angular coordinate system,  $(u, v)$ , where the origin is at the center of each lenslet. Since the pixels are surrogates for the angular sampling, they can obtain a range of the width of the primary optic. The image to the left of the FPA is one sub-aperture image. It is constructed by taking pixels at the same  $(u, v)$  position (in this case where the letters are,  $(-1 * \Delta u, -1 * \Delta v)$ ) and arranging the pixels based off of their lenslet position. The number of sub-aperture images and angular samples is equal to the number of pixels behind each lenslet, and the number of spatial samples is equal to the number of lenslets.

$$|F' - F| \leq \frac{\Delta x \Delta x}{\Delta p W_u} F' \quad (11)$$

Lastly, it is vital to discuss image formation inside the LFC and the refocusing algorithm. Although the angular sampling is considered a width of one section on the primary optic, it is measured by the FPA. Therefore a 4-D light field coordinate system is multiplexed onto a 2-D FPA, which is shown in Figure 6. In the figure, each colored square represents an area covered by a lenslet. Within each square is a circle, which is an image of the aperture created by the lenslet. The central lenslet to the

right of the FPA shows each colored square is labeled with an  $(x, y)$  coordinate with the origin at the center of the FPA and has a domain of the physical size of the FPA. Within each lenslet lies a separate coordinate system where each pixel corresponds to a  $(u, v)$  coordinate with the origin at the center of the lenslet and a domain of the physical size of the primary optic. To the left of the FPA is another view of the data called a sub-aperture image. In this view, the same  $(u, v)$  coordinate is taken from each lenslet and placed in the sub-aperture image grid based on their position of the microlens. It is essential to take note that the number of spatial samples of both the final image and sub-aperture images is equal to the number of microlenses in each dimension. There are also as many sub-aperture images as there are pixels behind each lenslet.

Inside the LFC, image formation takes the form of

$$E_{(\alpha * F)}(x', y') = \frac{1}{\alpha^2 F^2} \iint L_F^{(u,v)} \left( u * \left( 1 - \frac{1}{\alpha} \right) + \frac{x'}{\alpha}, v * \left( 1 - \frac{1}{\alpha} \right) + \frac{y'}{\alpha} \right) du dv \quad (12)$$

where  $L_F^{(u,v)}$  is the light field of a sub-aperture image,  $\alpha$  is the refocusing parameter where  $\alpha = F'/F$ , and  $x', y'$  are the new values for the spatial coordinates [25]. This integral can be approximated by shifting the sub-aperture images by  $u * (1 - 1/\alpha)$  and  $v * (1 - 1/\alpha)$  and adding them up as displayed in Figure 7. In this figure, only nine of the central sub-aperture images of the total 25 are used from Figure 6. In a)  $\alpha = 1$ , which corresponds to no shifts in the sub-aperture images. All of them are stacked on top of one another and summed up. In b), the sub-aperture images correspond to a shift of one lenslet among the central sub-aperture images. c) is the same as the previous picture but with a shift of two lenslets among the central sub-aperture images. The shift is based on its  $(u, v)$  position, and the only pixels that are added up are the ones within the central square in white. Typical ranges for the refocusing parameter  $\alpha$  to take are between 0.8 - 1.2. In the case of this study, the sub-aperture

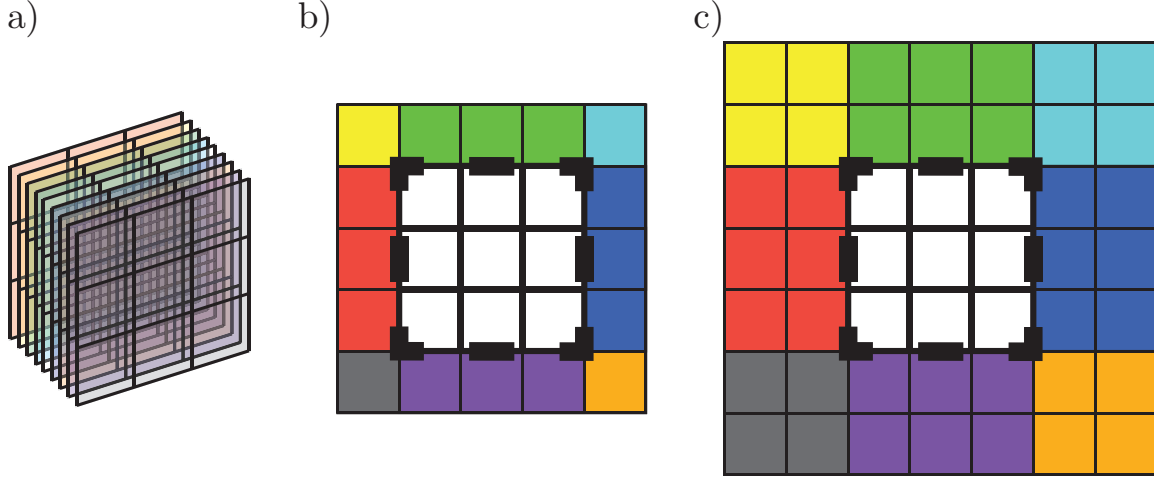


Figure 7. Visual representation of the shift-and-add algorithm using the central nine sub-aperture images of Figure 6. a) Refocusing algorithm when no shifting occurs. All sub-aperture images are stacked in the same spatial position and are added together to create the final image. b) Refocusing algorithm when there is a sub-aperture shift of one microlens. The pixels that are in the white square are the only ones that contribute to the final image formation. c) Refocusing algorithm when there is a sub-aperture shift of two microlenses.

images moved a maximum of about 17 lenslets.

### 2.3 Normalized Difference Vegetation Index

The Normalized Difference Vegetation Index (NDVI) is one of the earliest classification algorithms used for multi-spectral imagery. The index can be used for a variety of applications such as agriculture to measure biomass and precision farming. For forestry, the index can be used to determine forest supply as well as a leaf area index. Another use for the NDVI can be finding objects that are hiding or camouflaged inside areas of lots of vegetation. The equation to calculate an NDVI is displayed in equation 13 [3], which is based on the visible to near-infrared (NIR) reflectance spectra of vegetation shown in Figure 8.

$$\text{NDVI} = \frac{\rho(860 \text{ nm}) - \rho(660 \text{ nm})}{\rho(860 \text{ nm}) + \rho(660 \text{ nm})} \quad (13)$$

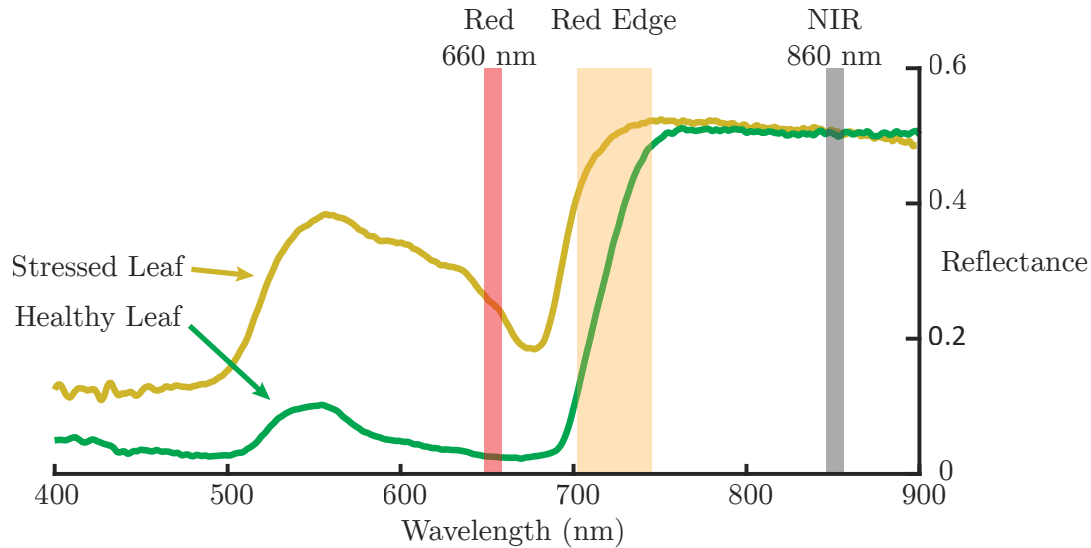


**Figure 8.** Typical visible to NIR reflectance spectra of a healthy and stressed leaf. In the visible, the reflectance is primarily characterized by low reflectance with a small increase near 550 nm. The low reflectance is caused by the absorption of the chlorophyll and other photosensitive parts of the leaf. As the reflectance transitions into the NIR, the reflectance experiences a sharp increase followed by a plateau. The transition from low to high reflectance is known as the red-edge. The high reflectance is due to water content and the structure of the plant. As the leaf becomes stressed, the red-edge blue-shifts due to the degradation of some of the chlorophyll. The spectral bands required to calculate an NDVI are shown by the red and grey bars.

where  $\rho$  is the reflectance at that spectral band.

Looking at Figure 8, it displays a typical visible to NIR reflectance spectra of vegetation, and for these spectra in particular it was taken of a single leaf. The visible part of the spectrum is characterized by low reflectance; this is caused by the absorption by photosensitive molecules like chlorophyll, xanthophylls, and phycobiliproteins [26], [27]. These molecules collectively absorb the most in the blue and red parts of the spectrum, which gives leaves and other vegetation their characteristic green color that we see. As the spectrum moves into the NIR, there is a sharp increase in reflectance; this transition region is called the red edge. The increase is strongly influenced by the volumetric scattering within the internal structure of the leaf and influenced by the content of water [28]. Therefore, if the scene contained multiple

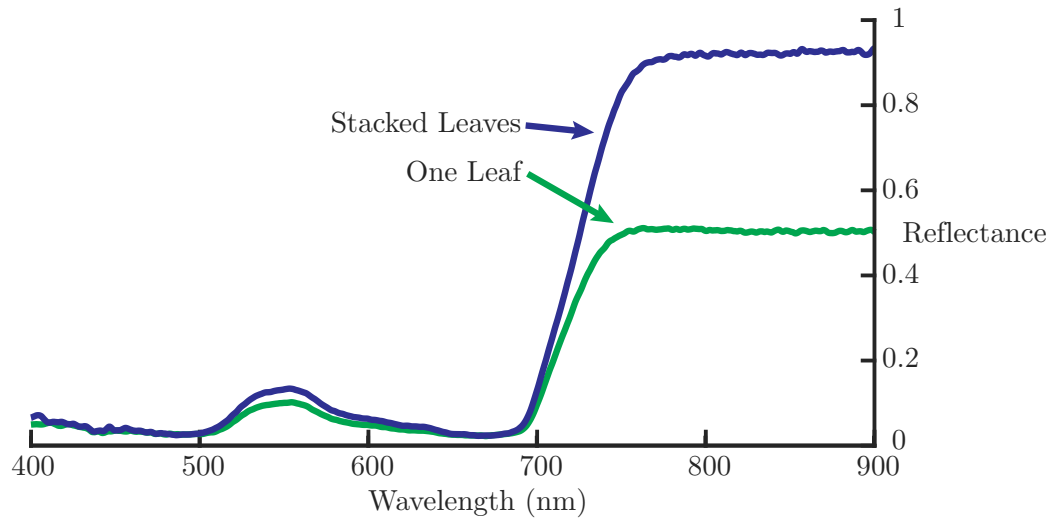


**Figure 9. The effect of multiple layers of leaves has on reflectance. Here the reflectance of one leaf is compared to the reflectance of seven leaves stacked upon each other. Due to the volumetric scattering of the internal structure of the leaf, the reflectance in the NIR dramatically increases with only a small increase in the visible.**

layers of vegetation such as a forest, this can dramatically increase the reflectance in the NIR, as demonstrated in Figure 9.

For applications like agriculture, techniques have been developed to determine the inflection point of the red edge which can be indicative of the health of vegetation [29]. As shown in Figure 8, if the leaf becomes stressed the red edge becomes blue-shifted. The cause of stress can be a wide variety of factors like water stress, absorption of heavy metals, defoliation, and chlorosis [30]. Regardless, as the leaf becomes further stressed, chlorophyll will degrade quicker than carotenes and xanthophyll, giving the leaves a yellowish-appearance. As the plant dies tannins will form, giving the leaves a brown appearance and decreasing the overall reflectance of the leaf [28].

Now that the spectra of leaves and vegetation have been discussed, the NDVI equation can be explained. The two bands required to take an NDVI are displayed graphically in Figure 8. It takes the reflectance from the NIR band, subtracts it by the red band, and normalizes it by the sum of the two. The NDVI can take

values that are between  $-1$  and  $1$ . Low values near  $0$  indicate barren features like rock or sand. Values near  $0.2$  or  $0.3$  correspond to features like plains or farmland, while higher values near  $0.7$  show dense forests or jungles. Negative values near  $-1$  from the NDVI are typically areas that contain water. From a remote sensing perspective, there are a few other factors that need to be taken into consideration when quantifying the presence of vegetation. Factors such as aerosol scattering and clouds can either reduce the amount of radiance coming to the sensor or prevent the signal from getting to the camera. Other noise factors may include contamination from the soil. If the ground contains moisture differences, organic matter differences, or roughness variations, there will be fluctuations within the NDVI. To account for these spectral variations, other indexes like the soil-adjusted vegetation index (SAVI) and atmospherically resistant vegetation index (ARVI) have been created [31], [32], but were not examined in this work.

### III. Theory

The diffractive plenoptic camera is functionally similar to that of a light field camera with a few fundamental differences. This chapter will serve as a way to describe how switching the refractive primary optic to a diffractive one affects its performance. The first section will create the design equations that were used to tailor the diffractive plenoptic camera used in this experiment to the required spectral bands to look at an NDVI. The second section will address some of the potential issues that may become a problem for multi-spectral imaging.

#### 3.1 Design Equations

To begin, Figure 10 displays how rays propagate and the placement of all the optics. The major setup difference between the DPC and the LFC in Figure 4 is that the MLA is placed a design focal length,  $f_0$ , away from the FZP. Previously, the object had some finite distance from the front optic and had to obey the thin lens equation

$$\frac{1}{s_0} + \frac{1}{s_i} = \frac{1}{f} \quad (14)$$

where  $s_0$  is the object distance from the lens,  $s_i$  is the image distance from the lens, and  $f$  is the focal length of the lens. In the case of the DPC, the object will either be at optical infinity or a constant depth. This way, the MLA can be placed at the proper distance, and any shift in the image plane will be due to the changes in wavelength, not object position. The  $(u, v)$  and  $(x, y)$  coordinates remain the same as the LFC. The image-side f-number matching is still required to prevent cross talk from other microlens images and to maximize the usage of pixels. For wavelengths other than design, the corresponding ray-space diagram is displayed in Figure 11. While similar to the LFC diagram, equation 4 describes how wavelengths shorter than design will

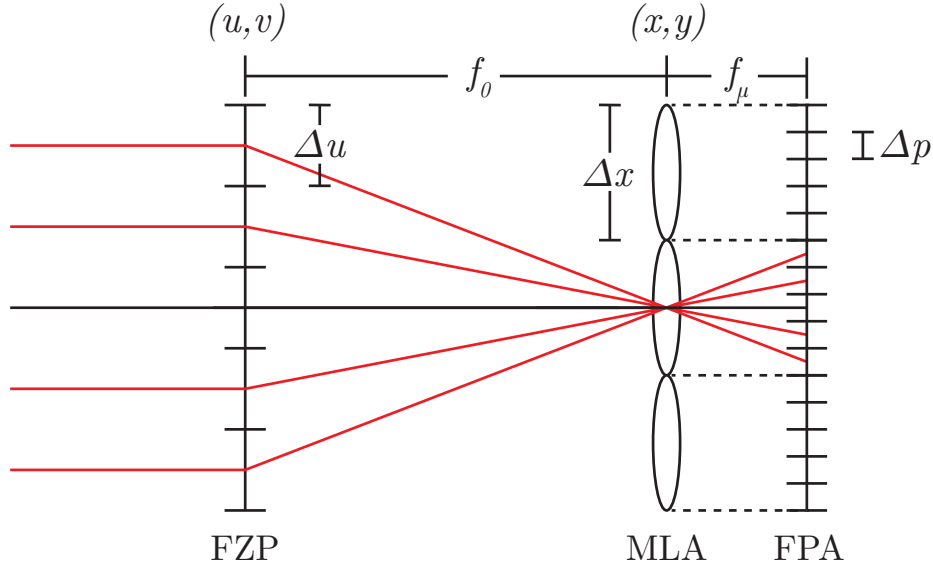


Figure 10. The basic setup and ray diagram of the DPC. The incident wavefront needs to be a planar wavefront or at a constant distance from the FZP, otherwise there is ambiguity between a change in wavelength or object depth. For objects at infinity, the MLA is placed at the design focus of the FZP and the FPA is placed at the focus of the MLA. The image-side f-number matching is still a requirement to ensure the image of the primary optic is only behind one lenslet. Each section the FZP is divided into is an angular sample,  $\Delta u$ , and corresponds to a pixel position,  $\Delta p$ , behind each lenslet. Each microlens gives a spatial sample,  $\Delta x$ , of the scene.

focus further which results in a positive slope. Similarly, wavelengths longer than design will focus closer and will result in a negative slope.

Now that the basic operation of the DPC has been explained, quantities of the FZP, MLA, and FPA will be placed in design equations to give a first-order approximation of what the performance of the DPC might be.

### Spectral Range.

The spectral range will be defined as the range of wavelengths that are capable of being digitally refocused without the loss of spatial sampling. This quantity will be derived by adapting Ng's "Perfect Digital Refocusing" Range in equation 11. The conditions behind the refocusing range begin by assuming the light field captured by the sensor is band-limited, which means the optical system captures a limited amount

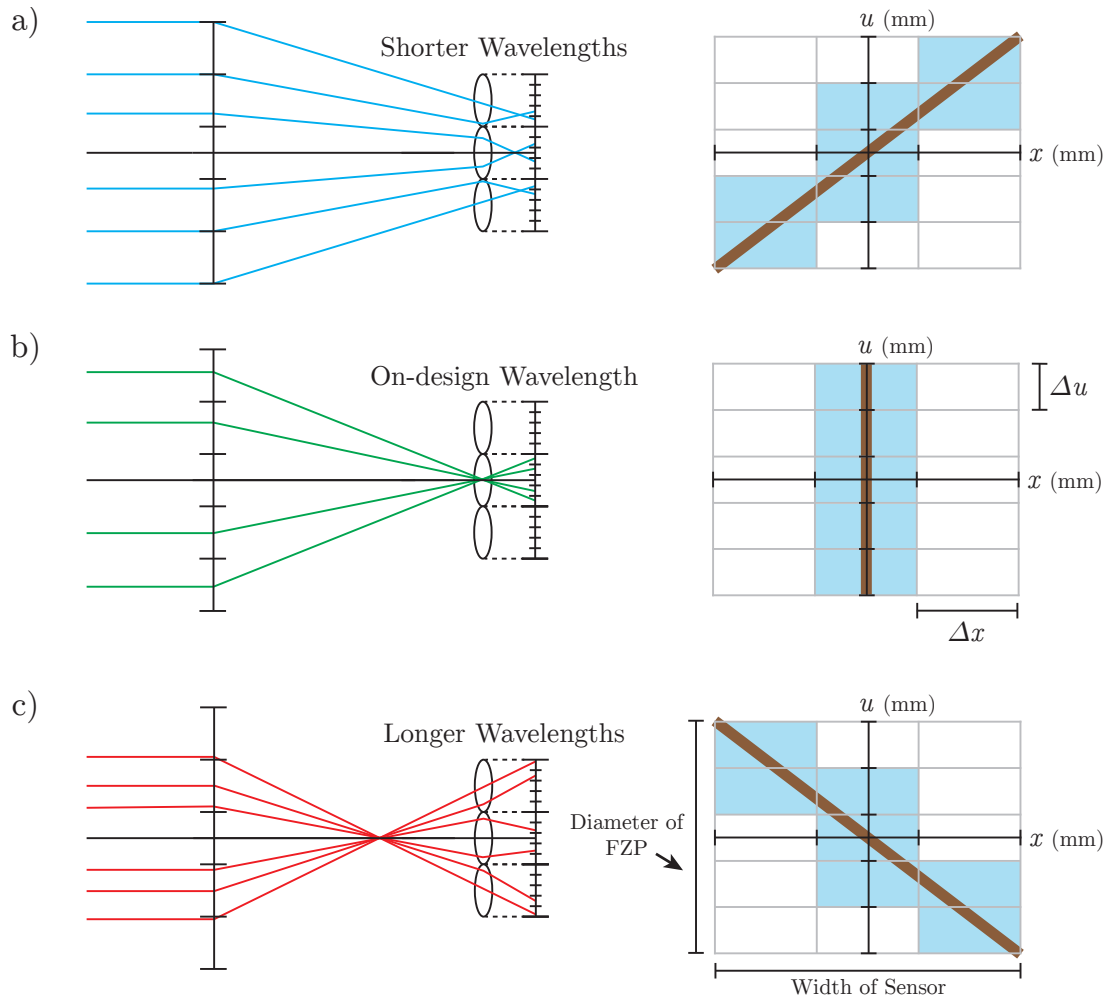


**Figure 11. The effect of wavelengths off-design and its graphical representation. Each color represents a different wavelength of light with green being the on design wavelength. The origin for the  $u$  coordinates is at the center of the FZP and the origin of the  $x$  coordinates are at the center of the FPA. a) For wavelengths shorter than design, the rays will still be converging as they impinge on the MLA and illuminate multiple lenslets. The resulting ray space diagram will have a positive slope. Each teal box is a discrete data point from the FPA and the brown line is the continuous data representation. b) The design wavelength will only illuminate one lenslet and result in a vertical slope. c) Wavelengths longer than design will focus closer than the MLA and results in rays diverging and illuminating multiple lenslets. The ray-space diagram results in a negative slope.**

of spatial frequencies in the  $(x, y)$  and  $(u, v)$  domains. Any signal captured within the limits of the spatial frequencies is sufficiently blurred that they match the spatial sampling of the MLA and the angular sampling done by the FPA. The range of depths

then that can be refocused should have the same Nyquist-sampled resolution as the original photograph [25].

To begin, the relative refocusing parameter  $\alpha$  will become  $\alpha = f_\lambda/f_0$  to fit the conventions of the DPC. Using equation 4 to substitute in for  $f_\lambda$ , will give the new relative refocusing parameter

$$\alpha_\lambda = \frac{\lambda_0}{\lambda} \quad (15)$$

where  $\lambda_0$  is the design wavelength of the FZP and  $\lambda$  is the incident wavelength. The number of spatial samples and the number of directional samples remain the same as in the LFC. By making the appropriate substitutions, an intermediate form of the “Perfect Digital Refocusing” Range for the DPC becomes

$$\text{Spectral Range} = |\lambda - \lambda_0| \leq \frac{\Delta x}{\Delta u} \lambda_0 \quad (16)$$

In this form, equation 16 says that the spectral range must be less than the ratio between the spatial sampling to the angular sampling. An example of increasing the spectral range without breaking the image-side f-number matching condition is to increase the number of pixels behind each lenslet. As the number of pixels increases, the angular sampling will decrease and the spectral range will increase. If the size of the spatial sampling changes, this will have an impact on the f-number matching condition and will change the angular sampling as well. To see how the f-number matching changes, the spectral range is displayed in equation 17.

$$\text{Spectral Range} \leq \frac{\Delta x}{\Delta p} \frac{f_\mu}{f_0} \lambda_0 \quad (17)$$

Here the equation can be further broken up by using similar triangles and substituting

in the definition of the f-number,  $f/\#$ , which gives

$$\frac{f_\mu}{f_0} = \frac{\Delta x f/\#}{f_0} \quad \text{or} \quad \frac{f_\mu}{W_u f/\#} \quad (18)$$

Equation 17 describes how changing the focal lengths relative to each other will affect the spectral range, but this will assume a certain f-number and width to the FZP. It is important to remember that the size of the lenslet will always be larger than the pixel and the focal length of the FZP will always be larger than the lenslet focal length. In this scenario, it would be advantageous to increase the lenslet size while trying to maximize the ratio of focal lengths. By breaking the ratio of focal lengths as in equation 18, it now assumes a certain focal length for either the lenslet or FZP in order to place it in terms of width and f-number. The last spectral range equation placed entirely in terms of widths is given by

$$\text{Spectral Range} \leq \frac{\Delta x}{\Delta p} \frac{\Delta x}{W_u} \lambda_0 \quad (19)$$

In this equation, it assumes the focal lengths of both the FZP and the lenslets. This is perhaps the most useful to understand how changing different quantities affect the range. The first term  $\Delta x/\Delta p$  expresses the ratio between the lenslet size to the pixel size. By adjusting the ratio, it describes how finely the light field is sampled in the ray space diagram and primarily affects the x-axis. The second term  $\Delta x/W_u$  is a ratio between the lenslet size to the FZP's width. This ratio gives the range of angles that the DPC can accept and will affect the y-axis of the ray space diagram. The structure of equation 19 is also similar to Ng's refocusing range in equation 11 with the exception that the DPC's version is in terms of the design wavelength instead of the off-design image distance  $F'$ .

An interesting note to add on here is in deriving all these equations, an explicit

form of the spatial-angular trade-off becomes apparent by multiplying  $\Delta u$  and  $\Delta x$  together to get

$$\Delta u \Delta x = W_u \Delta p \quad (20)$$

where  $W_u$  is the width of the FZP and  $\Delta p$  is the width of the pixel.

### Spectral Resolution.

The best overall spectral resolution the DPC can achieve is based on how well the FZP can resolve two irradiance peaks as explained in section 2.1. However, the spectral resolution will broaden due to spectral cross-talk from the zeroth-order of diffraction and wavelengths occupying the same spatial location, both of which are talked about in the next section. Furthermore, the spectral resolution will also broaden due to the refocusing algorithm itself. To get a first-order estimate on how well the DPC can resolve two wavelengths, incoming light will be considered to have negligible spectral cross-talk. Furthermore, the captured light field will be assumed to

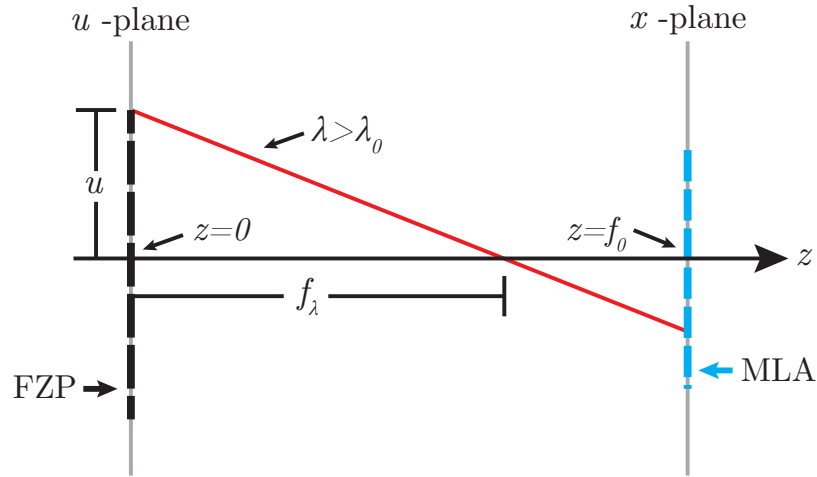


**Figure 12.** Ray diagram of how the  $u$  and  $x$  coordinates are related. Here the  $u$  and  $x$  planes are placed on the  $z$  axis and are separated by a distance  $f_0$ . The red line is a ray with longer than design wavelength and becomes refracted in front of the MLA. To find the equation for the red line, the slope is  $-u/f_\lambda$  and the  $y$ -intercept is  $u$ . Since the only plane of interest on the  $z$  axis is at the MLA,  $z = f_0$ . The equation for the line becomes  $x = -u\lambda/\lambda_0 + u$ .

be band-limited and can perfectly digitally refocus to wavelengths within the spectral range.

To begin, a relation between  $u$  and  $x$  needs to be established that is a function of wavelength. Figure 12 displays the  $u$  and  $x$  planes separated by a distance  $f_0$  with an incident off-design wavelength. The origin of the  $z$  axis will start at the  $u$  plane; the center of the FZP. For an incident ray of wavelength  $\lambda$ , it will impinge on the FZP at height  $u$  and become focused to a point  $f_\lambda$  and continue to propagate until it collides with the  $x$  plane; the MLA. The slope of this line becomes  $-u/f_\lambda$  and the intercept is  $u$ . The only  $z$  coordinate that is considered is at  $z = f_0$ , which gives the equation of a linear line to be

$$x = -\frac{u}{f_\lambda}f_0 + u \quad (21)$$

By substituting equation 4 for  $f_\lambda$ , equation 21 can now be expressed in terms of wavelength.

$$x = -\frac{u\lambda}{\lambda_0} + u$$

Ideally, the equation would be expressed in terms of  $u$  as a function of  $x$  and  $\lambda$  to create ray-space diagrams as shown in Figure 11. In doing so, the equation to relate the angular and spatial coordinates becomes

$$u = \frac{\lambda_0}{\lambda_0 - \lambda}x \quad (22)$$

The next step is to use equation 22, to create slopes for the ray-space diagram and to overlay the sampling grid on top of the slope to get a complete diagram as shown in Figure 13. In this figure, only the positive  $u$  and  $x$  values are displayed, with slopes of multiple wavelengths that are shorter than design. The incident wavefronts are normal to the FZP and are centered at the origin. In order for the DPC to detect

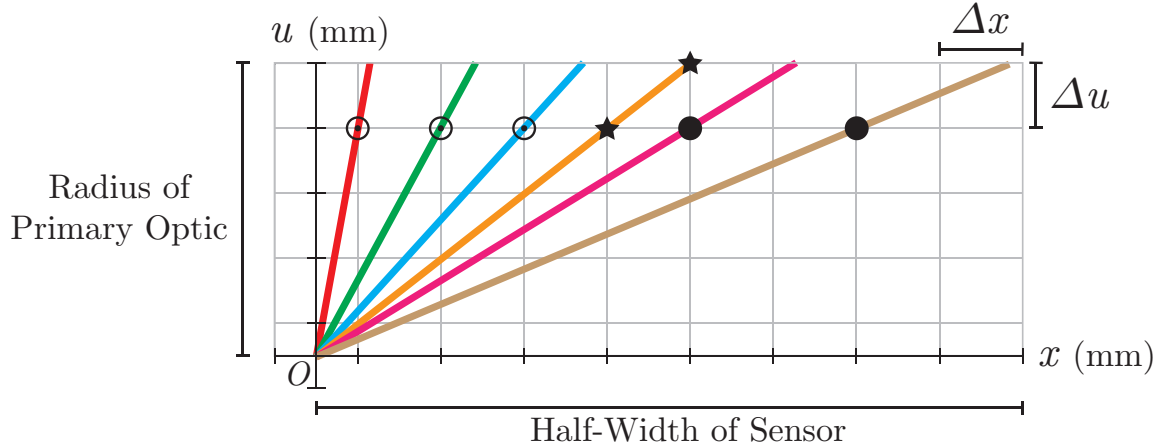


**Figure 13.** A quarter of the ray space diagram with multiple shorter incident wavelengths plotted. The spectral resolution is defined when one wavelength has one more microlens illuminated than the previous one. This condition is satisfied for lines drawn on the diagram. The lines with the dot in the center of the circle are wavelengths that are within the refocusing range. The line with the stars on it displays the last wavelength that is within the refocusing limit. The lines with a solid dot show wavelengths that are outside the refocusing limit and show that they require two lenslets in order to resolve them, which decreases the overall spatial sampling of the DPC.

a change from the design wavelength, the light must illuminate more than one lenslet. Similarly for the spectral resolution derivation, two wavelengths will be considered resolved when the light illuminates one more lenslet than the previous wavelength. This condition is plotted in Figure 13 in which each line plotted has one more lenslet illuminated than the previous one. The first three lines denoted by the circle with a dot in the middle display wavelengths that are close to the design wavelength and are within the spectral range of the DPC. As the wavelength moves further from design, there will be a point in which the light illuminates as many lenslets as there are pixels behind each lenslet. This is considered the end of the spectral range and is shown by the yellow line. By looking at equation 16, and rearranging it such that the spectral range is equal to  $\lambda_0/|\lambda_0 - \lambda| = \Delta u/\Delta x$ , it is directly related to the slope of the line drawn in the ray-space diagrams given by equation 22. The spectral range then says that the maximum slope that the DPC can sample without the loss

in spatial sampling is given by  $\Delta u/\Delta x$ . Figure 13 displays the end of the spectral range by denoting it with the stars on the yellow line, in which the slope is equal to the angular sampling over the spatial sampling. Beyond this range, wavelengths will spill onto two lenslets or more before they can be considered resolved, as shown by the lines with the solid black dot on them.

To get the spectral resolution, each slope that has one more lenslet illuminated than the previous one needs to be connected to a wavelength. Again, this condition occurs only at the circles with the dots in the middle of them and the stars. The rise for the slope for all these points is one angular sample below the width of the FZP:  $W_u/2 - \Delta u$ . The run for the slope will depend on how many lenslets from the origin are being lit up. In this case,  $m = 0$  will be considered the central lenslet on the origin of the  $x$ -axis while positive  $m$  values will be the lenslets to the right of the origin, and negative  $m$  values will be to the left. The run of the slope will then become  $\Delta x (1/2 + m)$ . By equating the slope in equation 22 to the discretized slope, the equation becomes

$$\frac{\lambda_0}{\lambda_0 - \lambda} = \frac{\frac{W_u}{2} - \Delta u}{\Delta x \left(\frac{1}{2} + m\right)} \quad (23)$$

The next step is to solve equation 23 for  $\lambda_0 - \lambda$ , which will give how far off from design the wavelength is.

$$d_m = \lambda_0 \left( \frac{\Delta x \left(\frac{1}{2} + m\right)}{\frac{W_u}{2} - \Delta u} \right) \quad (24)$$

where  $d_m = \lambda_0 - \lambda$ . Lastly, to get the change in wavelength between the two adjacent lenslets the difference must be found between  $d_{|m|} - d_{|m|-1}$ , where the absolute sign is placed there to prevent negative values for the spectral resolution.

$$\Delta\lambda = d_{|m|} - d_{|m|-1} = \lambda_0 \left( \frac{\Delta x \left(\frac{1}{2} + |m|\right)}{\frac{W_u}{2} - \Delta u} \right) - \lambda_0 \left( \frac{\Delta x \left(\frac{1}{2} + |m| - 1\right)}{\frac{W_u}{2} - \Delta u} \right)$$

By going through the algebra the spectral resolution becomes

$$\Delta\lambda = \frac{2\lambda_0\Delta x}{W_u - 2\Delta u} \quad (25)$$

and in terms of system parameters

$$\Delta\lambda = \frac{2\lambda_0\Delta x}{W_u \left(1 - 2\frac{\Delta p}{\Delta x}\right)} \quad (26)$$

This spectral resolution is only valid for wavelengths within the spectral range.

### Field of View.

The FOV of the DPC must be less than the limit set by the FZP in equation 8 in order to maintain good focus. Since the incoming wavefront is planar, the range of angles captured by the DPC is limited by the width of the sensor and the design focal length of the system. Thus, the FOV of the DPC is simply

$$\theta_{FOV} = \frac{W_x}{f_0} \quad (27)$$

where  $W_x$  is the width of the sensor, and the paraxial approximation is used. To determine the instantaneous FOV (IFOV) the range of angles are limited to a lenslet which gives

$$\theta_{IFOV} = \frac{\Delta x}{f_0} \quad (28)$$

## 3.2 Multi-Spectral Imaging

Up until this point, spectral cross-talk between bands has been neglected for the sake of simplicity. The two effects that cause cross-contamination are the zeroth-order of diffraction and the spatial-spectral overlay from the plenoptic camera. Both

problems affect the final output of the refocused image and cause false recorded irradiance values on the FPA.

### **Zeroth Diffraction Order.**

The zeroth diffraction order is unique to the DPC because the FZP allows a percentage of the incident light to pass through the plate unaltered. The undiffracted light looks like a plane wave to the MLA due to the short focal length of the lenslet. The MLA then refracts the light and creates an image on the FPA because the sensor is placed a lenslet focal length away. An example of this effect is shown in Figure 14. In this scene, the DPC's FOV was filled with an index card. When the image was processed through the shift-and-add algorithm, the resulting image was blank. In a), a magnified picture from the raw image of the sensor is shown. The light blue rectangle in each microlens image is the zeroth-order image of the scene, and it has a greater FOV than the DPC in the final image. The FOV of each lenslet is

$$\theta_{\mu FOV} = \frac{\Delta x}{f_{\mu}} \quad (29)$$

where  $f_{\mu}$  is lenslet focal length. b) displays all the sub-aperture images in their respective  $(u, v)$  location. The zeroth-order manifests itself by contaminating the central sub-aperture images.

The effect that it has on refocusing performance can be described by first imagining all the sub-aperture images stacked on top of one another, as displayed in Figure 7. The algorithm shifts the sub-aperture images according to  $u * (1 - 1/\alpha)$ . This means sub-aperture images that are not contaminated near edges with high  $u$  and  $v$  values will be the first ones shifted off and will no longer contribute un-contaminated values to the final refocused image. When the average of the spatial sample is taken, it will arbitrarily be higher because the uncontaminated values are no longer there to bring

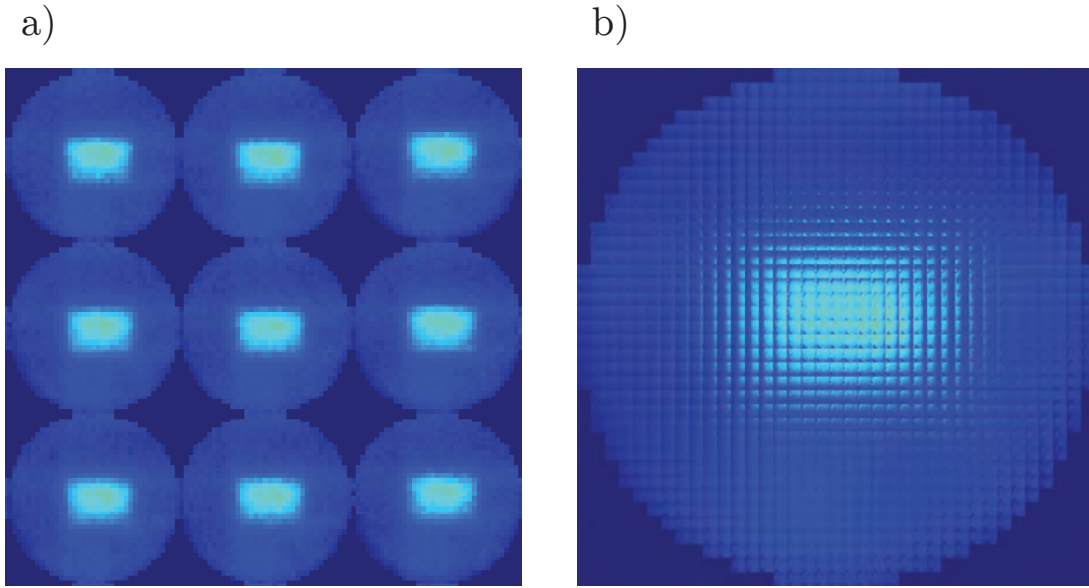


**Figure 14.** The effect that the zeroth diffraction order can have on image formation. Both images were obtained by filling the DPC's FOV with a blank index card so that when algorithm shifts-and-adds the sub-aperture images, the resulting refocused image is blank. a) Displays an arbitrarily magnified raw image of what the FPA sees. Each lenslet captures the zeroth diffraction order and images it onto the sensor. Despite filling the DPC's FOV with an index card, the zeroth-order image has a greater FOV. b) displays a sub-aperture view, which is a collection of all sub-aperture images in their corresponding  $(u, v)$  coordinates. The image of the index card behind each lenslet manifests its self by contaminating the central lenslets.

the average lower.

Another side effect of the zeroth-order is that it limits the dynamic range of the DPC. Looking at the diffraction efficiencies of the FZP in equation 9, the zeroth-order contains 25% of the energy while the first order only contains 10%. The zeroth-order will saturate the sensor at its microlens image before the first diffraction order saturates the pixels behind a microlens, thereby cutting its dynamic range.

### Spatial-Spectral Overlay.

The last issue that needs to be addressed is the spectral cross-talk that occurs when more than one wavelength is at the same spatial position. Figure 15 displays

an example of a planar wave with three spectral bands incident upon the DPC and the resulting FPA response. As expected, it focuses the design wavelength to one lenslet while the other wavelengths are spread out over multiple microlenses. All pixel positions are unique to their wavelength except the grey colored square in the middle. Here the pixels integrated all the wavelengths of light, leading to a higher digital number than any one pixel containing one wavelength. When the refocusing algorithm is applied, this can lead to false high values for wavelengths that should have little to no contribution. The spatial-spectral overlay is also the reason why there must be spatial variation in the scene. Otherwise, there will be no change in the sub-aperture images leaving every shift to be the same

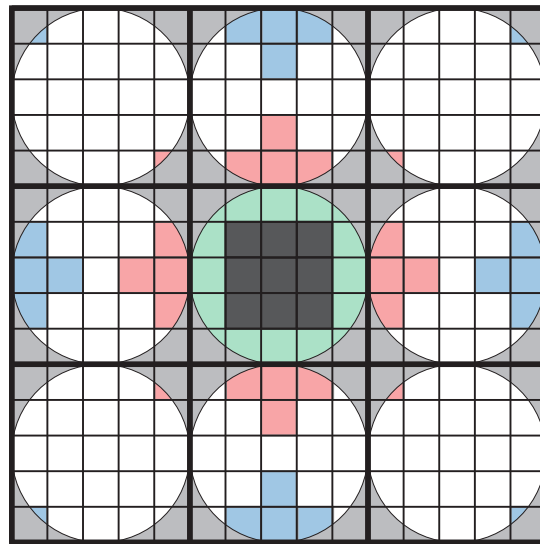


Figure 15. Spectral cross-talk when a multi-spectral object occupies the same spatial position. In this example, there is a point source that contains three wavelengths: green (on design), blue (shorter than design), and red (longer than design). In the central lenslet, the square in the middle contains all three integrated spectral values which are grey while all the other pixels are unique for their spectral value. When the raw array is transformed into a sub-aperture array, the contaminated pixels will contribute a higher digital number in the final summation leading to a false value.

## IV. Experiment

This thesis provides an experimental demonstration of the DPC as a snapshot multi-spectral camera looking at an NDVI. The design equations derived in the previous chapter were used to develop the DPC to look at the spectrum of a leaf. The spectral resolution of the system was tested to verify the design equation's validity. Also, the DPC will be used to calculate the reflectance of the scene to calculate an NDVI. The first section will explain the creation of the DPC and its calibration, while the second section will explain the two test profiles of the experiment.

### 4.1 DPC Construction

#### Fresnel Zone Plate Design and Fabrication.

The FZP was created to accommodate a spectral range of 120 nm from the design wavelength of 770 nm. This encompasses the entire spectral range required to calculate an NDVI with room for error. The image-side f-number of the FZP was 10.02 to match the f-number of readily available MLAs in the lab. The f-number of the FZP was also made slightly larger than the MLA to ensure the lenslet images did not overlap one another, which allowed for a better calibration of the lenslet position.

The FZP was designed using MATLAB, which encoded a GERBER file format and was manufactured by Advance Reproductions. The resulting parameters of the FZP used in this thesis are placed in Table 1. The FZP was placed on a single 4in x 4in quartz plate coated with a 0.09 mm thick chrome layer. The smallest ring on the FZP was  $7.71 \pm 0.15 \mu m$ .

**Table 1.** Design parameters that were used to manufacture the FZP with a tolerance of  $\pm 0.15\mu m$

$\lambda_0$ (nm)	$f_0$ (mm)	$W_u$ (mm)	$f/\#$	# of Rings, N
770	267.26	26.68	10.02	864

### Microlens Array and Board Camera.

The MLA was chosen to minimize the size of each lenslet to maximize the spatial sampling and to keep the image side f-number matching between the MLA and FZP. Any f-number lower than 9.5 would not allow the MLA to get close enough to the FPA. The MLA was purchased from RPC Photonics and is made up of polymer-on-glass material with a thickness of 2 mm. The MLA parameters used in this thesis are displayed in Table 2. The MLA had a transmission spectrum greater than 0.9 between 400 – 2000 nm with a square geometry and a nominal fill factor of 100%.

**Table 2.** Microlens array parameters

$f_\mu$ (mm)	Lenslet size, $\Delta x$ (mm)	$f/\#$
0.95	0.10	9.5

The board camera used was a SONY IMX178LLJ purchased from The Imaging Source. It is a monochrome CMOS image sensor with 3072 x 2048 pixel sampling with a spectral sensitivity ranging from 400 nm to 1000 nm and a pixel size of 2.4  $\mu m$ . The FPA parameters are displayed in Table 3.

**Table 3.** Focal plane array parameters

Pixel Count	Pixel Size, $\Delta p$ ( $\mu m$ )
3072 x 2048	2.4

The mount for the board camera was a custom-built, 3D printed backing displayed in Figure 16. The mount allowed for screws and springs to be attached to the board camera, which enabled the tip and tilt of the sensor. This was useful for the precise alignment of the sensor to be flat relative to the MLA.

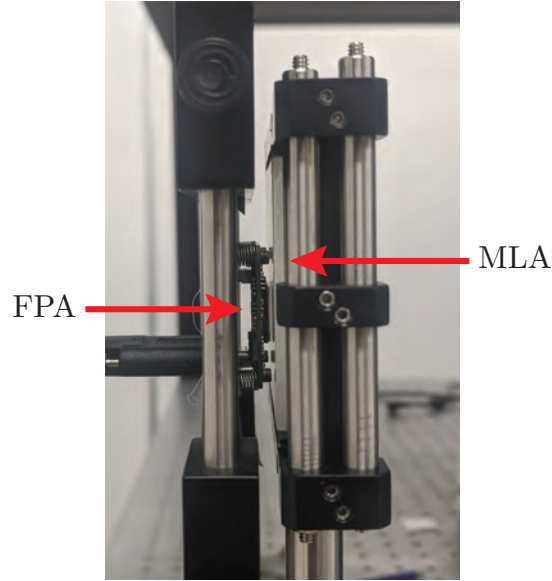


**Figure 16.** Experimental setup of MLA and FPA used in all experiments. The FPA is attached to a custom-built 3D printed backing, which connects the sensor to a set of springs and screws. The adjustment of the screws allows the sensor to be tilted to be flat relative to the MLA. Additionally, this picture shows that the MLA and FPA are almost as close as they can get without the two physically touching.

### **DPC Calibration.**

The calibration of the DPC ensures that the center of each lenslet is found, and a proper refocused image occurs. To begin, a Spectra-Physics 3900S tunable continuous-wave Ti:Sapphire laser was set to the design wavelength of the FZP, as shown in Figure 17. The laser intensity was controlled with a variable ND filter to prevent damage to the sensor. A spatial filter (SF) with a microscope objective of 11 mm was used to focus the laser to a  $10\ \mu\text{m}$  pinhole and collimated by a 200 mm lens (L1). A shear plate was used to ensure the beam was adequately collimated.

Next, the FZP was removed to get the correct spacing between the MLA and FPA. Using a live feed from the FPA, the separation between the MLA and FPA was adjusted until an image of a small point was formed behind each lenslet. Afterward, the digital counts of the points were compared at the corners of the FPA. Ideally, the

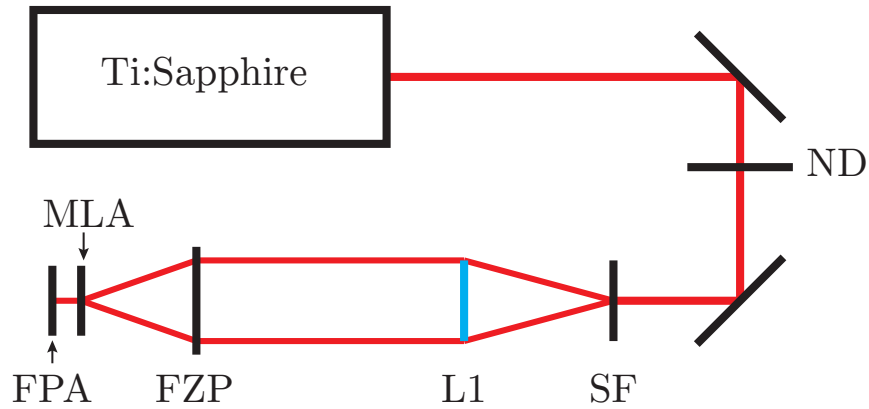


**Figure 17. Laser setup for DPC calibration and spectral resolution test profile. A laser beam from a Ti:Sapphire crystal with a tuneable range of 700 nm to 850 nm is emitted and attenuated using a variable ND filter. The laser continues to propagate into the spatial filter (SF) with a microscope objective focus of 11 mm and a pinhole of 10  $\mu\text{m}$ . The beam is collimated using a 200 mm lens (L1). The laser continues propagating until it is incident upon the DPC system. The FZP is removed to determine the correct distance from the MLA to the FPA.**

points will be uniform in intensity and follow straight lines across the FPA. If the points display different intensities at the corners, the FPA and MLA are not parallel to each other. This was fixed by using the screws attached to the FPA and adjusting until both were parallel. If the points are generally climbing higher or lower on the sensor, the FPA is rotated with respect to the MLA. Once the points were evenly illuminated and the tilt was fixed as best as it can, the FZP was placed back into the system. The FZP distance to the MLA was adjusted until the laser focused down to the center lenslet. Once this was complete, the DPC was ready for imaging at infinity. For point to point imaging, the target was illuminated with the design wavelength and the FZP distance to the MLA was adjusted until a sharp image formed on the FPA using the live feed.

After the optical elements were placed at the correct distances, the centers of each lenslet were found in order to sample the light field correctly. To determine the

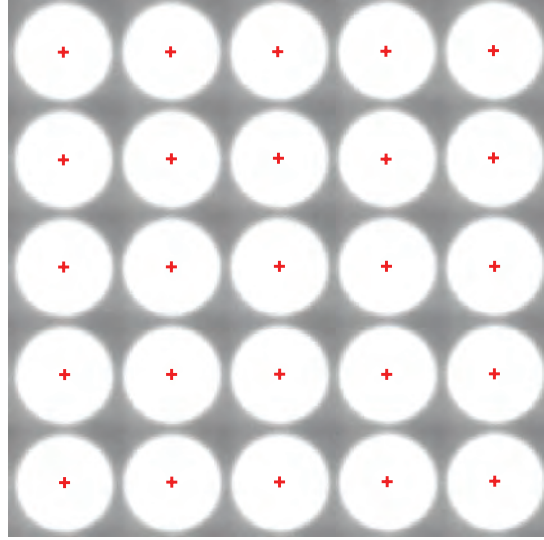


**Figure 18.** Detection of the centers of each lenslet. This figure is an arbitrarily magnified view of a raw image captured from the FPA without any refocusing. To get this image, a bright lamp was placed within the DPC's FOV which illuminated all the lenslets. Each lenslet imaged the aperture of the system onto the FPA which are the circles shown here. The FPA-captured image is then placed into MATLAB's *imfindcircles* function, which determines the center of each lenslet as displayed by the red crosses.

center of each microlens, a bright white source was placed within the DPC's FOV. The live-view from the FPA showed a grid of circles, which are images of the circular aperture from the FZP. A picture was taken of the array of circles and MATLAB's *imfindcircles* function was used. The function detects the centers of each circle using a circular Hough transform as shown in Figure 18 [33]. From here, spot corrections were done to delete false centers or add in missed lenslets. It is crucial to collect accurate lenslet position as it will significantly impact how the light field is reconstructed in the refocusing algorithm.

The next step is to take the data collected from the raw image of the FPA and re-sample it onto a uniform  $L(u, v, x, y)$  grid. I used the function *interpimage2* from the Light-Field Imaging Toolkit and adjusted it to our needs [34]. This step will correct the imperfect alignment of the FPA to the MLA and the variability in the

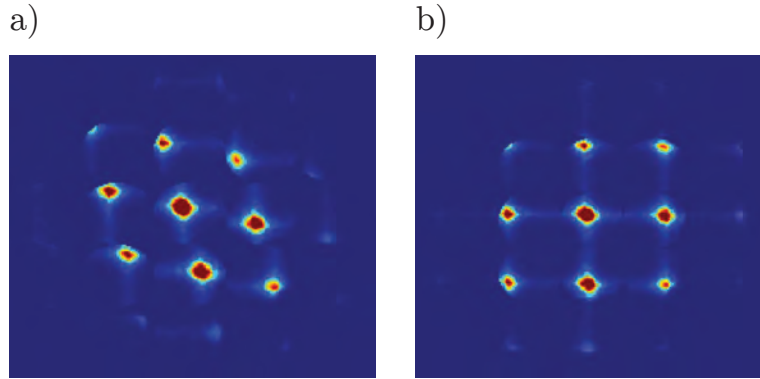


**Figure 19.** This example displays how sensor tilt with respect to the MLA is sampled. a) Once the centers of each lenslet are found, they are more than likely to not be in a straight line due to experimental error or circle detection error. If a refocused image were made using this image, there would be a slight tilt to it. b) by re-sampling the raw sensor data to a uniform  $(u, v)$  grid, the resulting refocused image will not be skewed.

detection of each lenslet's center. If this step is not done, the raw FPA image will have a slight slant to it after it has been sampled through the algorithm as displayed in Figure 19. Additionally during this step, a circular mask is applied to each lenslet image. Looking at Figure 18, areas that are outside the circular lenslet image are still sampled into the light field because it is a square lenslet, but they only contribute noise to the final image. By zeroing these areas out, it will prevent background noise contribution and will only sample the aperture as shown in Figure 14 picture a).

The last step is to control vignetting that occurs as the algorithm refocuses to wavelengths other than design. During the refocusing process, all the sub-aperture images are stacked on top of one another and added as displayed in Figure 7. As the algorithm shifts the sub-aperture images, there will be fewer sub-aperture images stacked on a specific pixel in the refocused image, particularly near the corners. Also, there will be some sub-aperture images that do not contribute at all because they fall outside the aperture of the DPC, which is shown in the corners of Figure 14 picture b). To account for the unequal amount of sub-aperture images stacked on a single

refocused pixel, the pixel value is normalized to the amount of contributing (values that are greater than 0) sub-aperture images stacked on that pixel.

There are a few techniques that can be used to verify that the correct center of each lenslet was found and re-sampled onto a uniform  $L(u, v, x, y)$  grid. The first technique is to display the raw FPA image after it has been through the center detection and re-sampling process. To do this view, keep the spatial coordinates  $(x, y)$  constant and let the angular coordinates  $(u, v)$  vary. By doing this, it takes the re-sampled pixels from the FPA and places them behind their correct lenslet as shown in Figure 20 in the left column. Comparing the re-sampled data to the original raw FPA image, it is obvious when there is an incorrect detection of the centers as an image of the aperture appears to be cut off. Both of these images also show that the mask is zeroing out areas outside the aperture and reducing the space between each lenslet image to account for the slight f-number mismatch.

The next technique to verify a good lenslet calibration is to place the re-sampled data into a sub-aperture view. This view is the same one as described in Ng's dissertation on page 30, figure 3.5 [25], where the angular coordinates are held constant and the spatial coordinates vary. In this view, it displays all the sub-aperture images in their corresponding  $(u, v)$  location on the primary optic. For a bad calibration in the middle column of Figure 20, some of the sub-aperture images are blank within the DPC's FOV. However, this is incorrect because each sub-aperture image should contain an image of the scene from different perspectives. Additionally, a red box is placed at what is supposed to be the central sub-aperture image  $(u, v) = (0, 0)$  and show the differences in the sub-aperture quality in the right column. For both calibrations, they produce a relatively sharp image of the square however, the bad calibration picked up more noise around the surrounding area of the square than the good calibration. Now because the bad calibration can still create sharp pictures

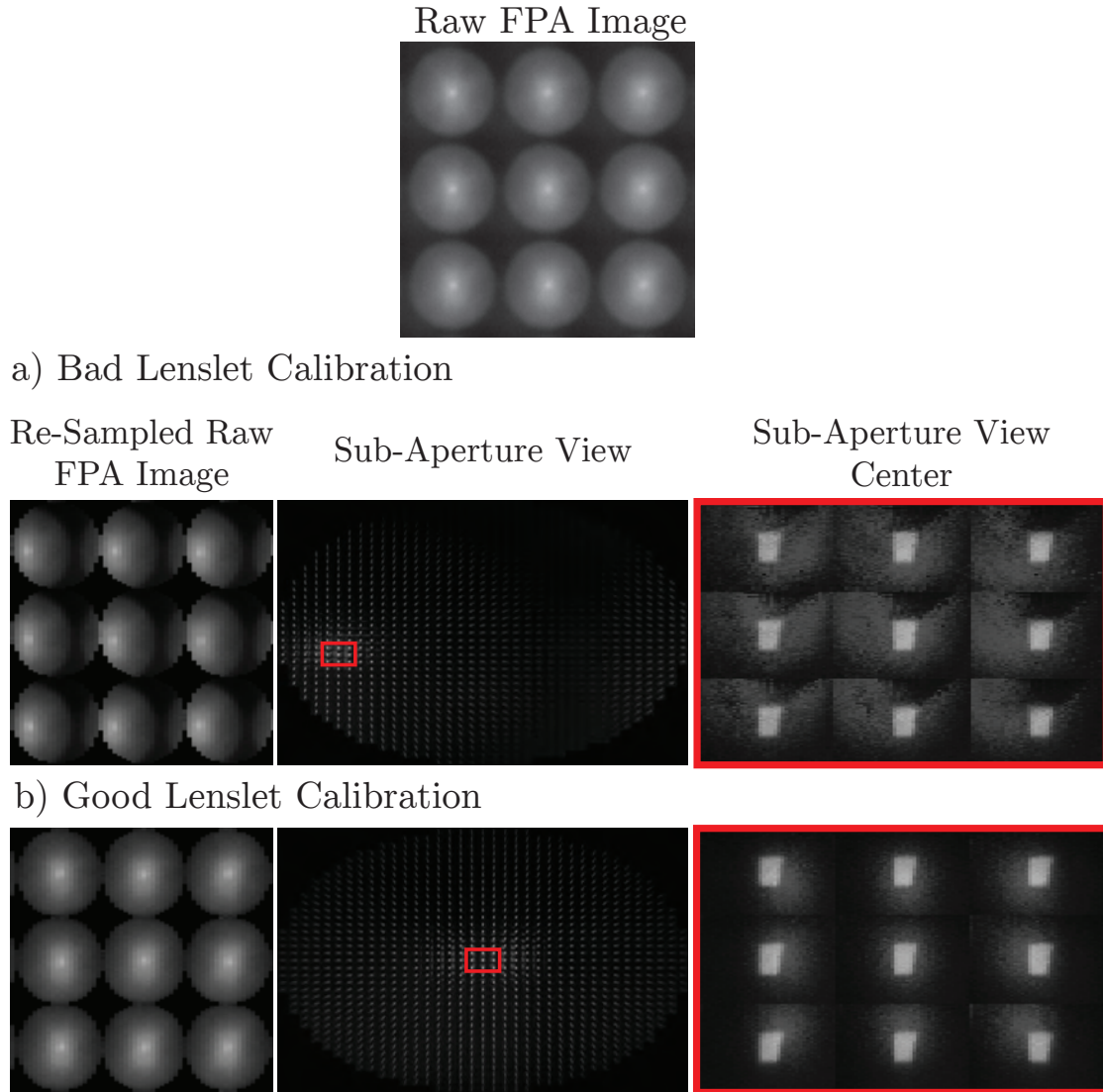


Figure 20. Methods to verify if the center of each lenslet was correctly detected. On the top is an arbitrarily magnified view of an image taken by the FPA without any alteration. The left column is the same magnified view of raw FPA image, but the centers of each lenslet were found and re-sampled to build a uniform  $L(u, v, x, y)$  grid. The middle column is a sub-aperture view built from the re-sampled data and has what should be the central sub-aperture images boxed in red. The right column contains a magnified view of the sub-aperture images boxed in red in the middle column. a) contains images that have incorrect centers found for each lenslet while b) provides the correct centers.

somewhere within its sub-aperture images, the final refocused image may still look like the scene. However, as the algorithm shifts and adds, the final image will not

refocus correctly.

Finally, to verify the refocusing algorithm is refocusing to the correct spectral band a simple test can be conducted. The easiest method is to image a target illuminated with monochromatic light or image a collimated beam from a laser and refocus to that spectral band. The final refocused image should be of that object for a target or a single pixel for the collimated beam. If the image refocuses more sharply for wavelengths other than what was illuminated, the optics may need to be further adjusted to correspond with the correct  $\alpha$  value.

The resulting DPC parameters after performing the above calibration and verification steps are displayed in Table 4

**Table 4. DPC parameters from design equations and resulting spatial and angular sampling**

$\Delta\lambda$ (nm)	$\theta_{FOV}$	Spectral Range (nm)	$N_x$	$N_y$	$N_u, N_v$
6.06	1.58°	120.23	73	47	37

## 4.2 Test Profiles

### Spectral Resolution.

The spectral resolution of the system is a measure of how well the DPC can resolve two separate wavelengths from one another. In this particular setup, effects from the zeroth-order are considered negligible because the spread of the zeroth-order image is uniform and can be subtracted from the image. Additionally, the setup will be imaging one wavelength at a time which renders the spatial-spectral overlay noise to become negligible. The outcome of this experiment will give a sense of how well the refocusing algorithm can take a raw image with a wavelength other than design and refocus it back to one pixel in the final refocused image.

The setup of the experiment will have the same layout as in Figure 17 with the

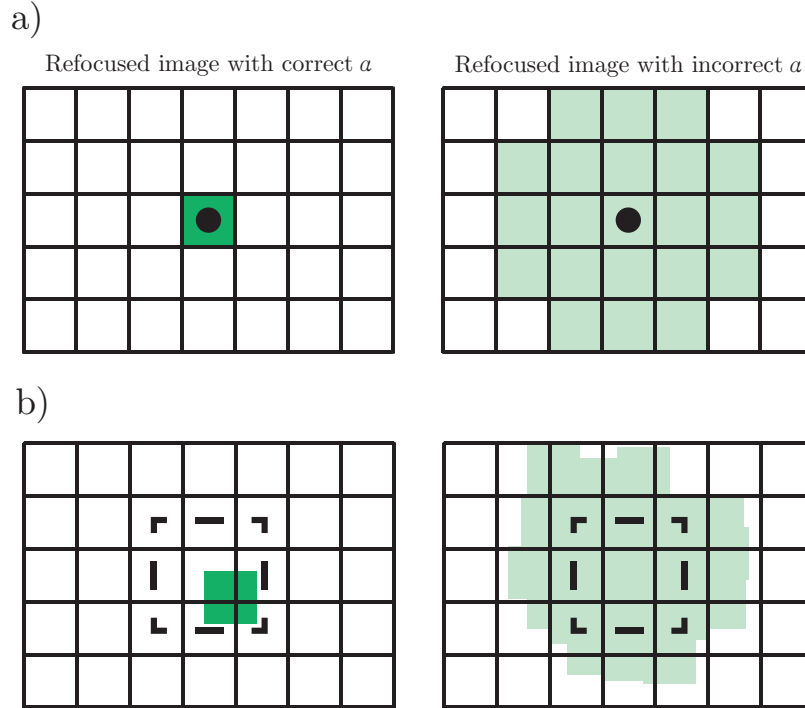


Figure 21. a) displays an ideal scenario of what a refocused-image should be sampled as. For an  $\alpha$  value that corresponds to the correct wavelength, the refocused image should become a sharp point and fill one pixel as shown on the left. For values of  $\alpha$  that do not correspond with the proper wavelength, the refocused images will be a blur of low values displayed on the right. To determine how well the algorithm can bring a planar wave of a particular wavelength down to a single point, the irradiance of the peak pixel location is found and held constant as the  $\alpha$  parameter is varied. In the case of a), the location of the peak pixel value is found on the left and marked with a solid dot. As the refocusing parameter is changed as shown on the right, the dot remains in the same location. However, due to imperfect beam collimation, uneven distribution of power of the laser, and other experimental errors, the refocusing performance will look more like part b), where the center of the beam may land in between pixels. The imperfect refocusing will decrease the amount of irradiance received if only one pixel was tracked. Instead, a 3 x 3 square is tracked and integrated around the location of the peak pixel location as shown by the dotted square on the left side. The location will be held constant and will continue to integrate the same location as  $\alpha$  varies.

addition of an EG&G Model 450 radiometer with a spectrally-flat filter attachment. The attachment will ensure that the radiometer is equally responsive to all wavelengths within a region. To test the spectral resolution of the DPC, the Ti:Sapphire laser beam will be tuned to different wavelengths, collimated after the spatial filter, and enter the DPC. With each change in wavelength, the amount of optical power

will be checked with the radiometer to keep the power on the DPC consistent. In the experiment, the radiometer was kept to a value of  $330 \mu W/cm^2$ , while the sensor was kept at a constant integration time of  $1/6211$  sec to prevent saturation.

Next, each photo of a monochromatic laser beam will be digitally refocused to all wavelengths within the refocusing range to form a point and blur as shown in Figure 21. However, due to imperfect beam collimation, uneven distribution of power, and the algorithm itself, the point may not land perfectly on one pixel of the refocused image. Instead, it can land in-between pixels will and may be more of a blur of multiple points as shown in part b). To account for this, the highest pixel in all of the refocused images is found and the location is recorded. A  $3 \times 3$  square is formed around the highest pixel as displayed by the dotted line in Figure 21 part b), and integrated for that image. The location of the square is held constant, and it will continue to integrate for other values of alpha. Each stack of integrated values will be compared to one another and will be considered resolved by using Sparrow's criterion. This criterion considers two peaks resolved when the "undulation" condition is achieved and can hold for unequal peaks whose ratios are less than 10:2 [35].

### **Reflectance and NDVI Measurement.**

The purpose of this experiment is to test the multi-spectral imaging capabilities of the DPC and to see how the described noise sources affect the measurement in comparison to a grating spectrometer. To begin, in order to correlate the digital numbers to reflectance, a thorough treatment of the radiometry needs to occur. The geometry of the measurements to collect the reflectance data is shown in Figure 22. In a) a 90-watt spotlight was placed approximately 51.2 cm from the sample holder at the same height at an angle of  $58.1^\circ$  from the surface normal of the holder. The lamp was placed at a steep angle to minimize the specular reflection from the uneven

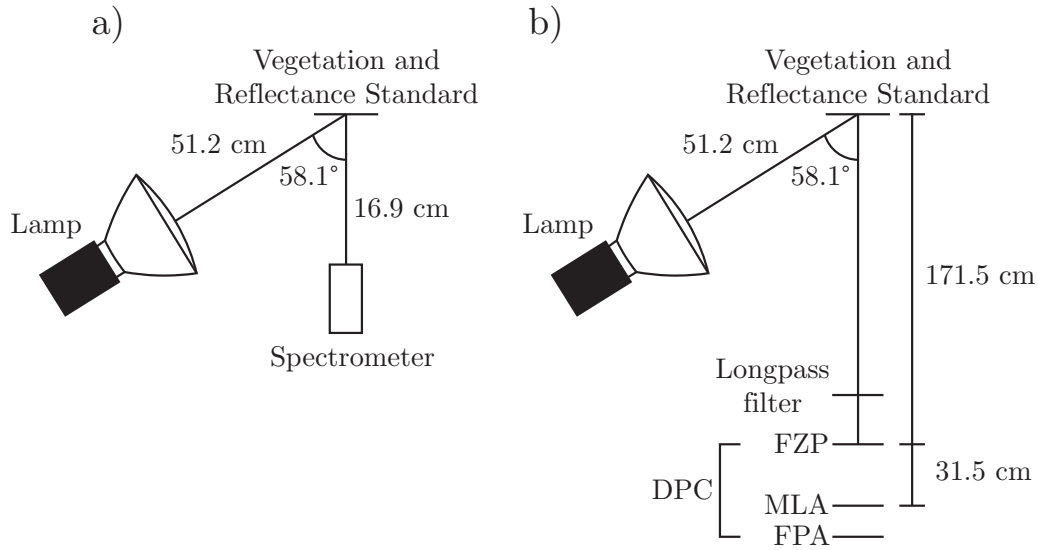


**Figure 22. Reflectance measurement setup for the spectrometer and DPC. a) The lamp is placed at a steep angle from the normal to reduce specular reflection for vegetation measurements. The spectrometer's FOV was filled with the measured object and placed far enough away to prevent saturation. b) The lamp and measured objects remained in the same location and placed far enough away to only cover part of the DPC's FOV. The DPC was configured for point-to-point imaging by adjusting the distance from the FZP to the MLA to capture the new focus of the design wavelength. A longpass filter with a cut-on wavelength of 650 nm was placed in front of the DPC to reduce noise from shorter wavelengths.**

surfaces of the leaf. A BWTEK BRC115P-V-VIS/NIR spectrometer was placed 16.9 cm from the holder with its FOV filled with the sample and placed far enough away to prevent saturation. In b) the lamp and sample holder were kept the same as the spectrometer measurements. The DPC was set up for point-to-point imaging due to the space limitations of the lab table. The DPC was placed approximately 171.5 cm away from the sample holder and the distance from the FZP and MLA was 31.5 cm. A longpass filter with a cut-on wavelength of 650 nm was placed in front of the DPC to reduce noise from shorter wavelengths to which the sensor was more sensitive to. The reflectance standard used in this experiment was a Spectralon® standard from Labsphere and the vegetation used was leaves in various states of health.

In order to measure the reflectance of the sample, the amount of flux received

by the sensor needs to be determined. To begin the analysis of the radiometry, the amount of flux incident upon the sample from the lamp is defined as

$$\Phi_e^{inc} = L_e^{lamp} A_{lamp} \Omega_{lamp}$$

where  $\Phi_e^{inc}$  is the incident flux on the sample from the lamp,  $L_e^{lamp}$  is the radiance of the lamp,  $A_{lamp}$  is the area of the lamp, and  $\Omega_{lamp}$  is the solid angle subtended by the sample.  $\Omega_{lamp}$  can be decomposed into  $\frac{A_{Samp} \cos(\Theta)}{R^2}$  where  $A_{Samp}$  is the area of the sample and  $R$  is the distance between the lamp and the sample. The area of the sample is divided on both sides to get the incident irradiance  $E_{inc}$

$$E_{inc}(\lambda) = \frac{L_e^{lamp}(\lambda) A_{lamp} \cos(\Theta)}{R^2}$$

where  $\Theta$  is the angle between the surface normal of the sample and the direction of the lamp. The exitance reflected by the sample's surface then becomes

$$M_{refl}(\lambda) = E_{inc}(\lambda) \rho(\lambda)$$

where  $M_{refl}$  is the exitance of the reflected light and  $\rho(\lambda)$  is the spectral reflectance of the sample. Here it is assumed that both the reflectance of the scene and the standard are Lambertian in order to calculate the reflected radiance,  $L_{refl}$

$$L_{refl}(\lambda) = E_{inc}(\lambda) \frac{\rho(\lambda)}{\pi}$$

While the leaf may not be entirely Lambertian due to the uneven surfaces, the approximation will be used to get a first order estimate of the reflectance. The amount

of flux arriving at the detector from the sample  $\Phi_e^{refl}$  will become

$$\Phi_e^{refl}(\lambda) = L_{refl}(\lambda) \Omega_{FOV} A_{opt} t_{opt} \mathcal{R}_{Sen}(\lambda)$$

where  $\Omega_{FOV}$  is the solid angle FOV of the detector,  $A_{opt}$  is the area of the detector's optic,  $t_{opt}$  is the transmission of the optics, and  $\mathcal{R}_{Sen}(\lambda)$  is the responsivity of the sensor. By doing the proper substitutions for  $L_{refl}$  and  $E_{inc}$ ,  $\Phi_e^{refl}$  becomes

$$\Phi_e^{refl}(\lambda) = \frac{L_e^{lamp}(\lambda) A_{lamp} \cos(\Theta) \rho(\lambda)}{R^2} \Omega_{FOV} A_{opt} t_{opt} \mathcal{R}_{Sen}(\lambda) \quad (30)$$

This equation gives the relation between the flux received by the sensor and the reflectance of the samples. To find the reflectance of vegetation,  $\rho_{Veg}$  we solve equation 30 to get

$$\rho_{Veg}(\lambda) = \Phi_e^{Veg}(\lambda) \frac{R^2}{L_e^{lamp}(\lambda) A_{lamp}} \frac{\pi}{\Omega_{FOV} A_{opt} t_{opt} \mathcal{R}_{Sen}(\lambda) \cos(\Theta)}$$

where  $\Phi_e^{Veg}$  is the flux received by the sensor of vegetation. However, in order to calculate  $\rho_{Veg}$  the radiance of the lamp,  $L_e^{lamp}$ , needs to be known. To do this, a Spectralon<sup>®</sup> reflectance standard was placed at the sample location and a measurement was taken. Since the reflectance of the Spectralon<sup>®</sup> is known, the radiance of the lamp becomes

$$L_e^{lamp}(\lambda) = \Phi_e^{Std}(\lambda) \frac{R^2}{A_{lamp} \Omega_{FOV} A_{opt} t_{opt} \mathcal{R}_{Sen}(\lambda) \cos(\Theta)} \frac{\pi}{\rho_{Std}(\lambda)}$$

where  $\Phi_e^{Std}$  is the flux from the reflectance standard and  $\rho_{Std}$  is the reflectance of the Spectralon<sup>®</sup>. By substituting  $L_e^{lamp}$  into  $\rho_{Veg}$  and doing the proper algebra, the

reflectance of vegetation becomes

$$\rho_{Veg}(\lambda) = \frac{\Phi_e^{Veg}(\lambda)}{\Phi_e^{Std}(\lambda)} \rho_{Std}(\lambda) \quad (31)$$

In terms of values that are measured by the spectrometer or the DPC, the reflectance becomes

$$\rho_{Veg}(\lambda) = \frac{DN_{Veg}(\lambda)}{DN_{Std}(\lambda)} \rho_{Std}(\lambda) \quad (32)$$

where  $DN_{Veg}$  is the digital number measured for vegetation and  $DN_{Std}$  is the digital number measured for the reflectance standard provided measurements stayed within the linear response of the sensor. The radiometry is the same for the DPC and spectrometer, but with the DPC it is done on a pixel-by-pixel basis. The value for  $DN_{Std}$  used for the DPC was an average over the entire area of the Spectralon<sup>®</sup> in each refocused image while  $DN_{Veg}$  was an individual pixel within the refocused image. After the reflectance measurement is complete, an NDVI will be calculated for the grating spectrometer and the DPC.

The three scenes were picked in a way to give different values for the NDVI as shown in Figure 23. Here the three leaves are in various states of health: The first is a deep green leaf without any signs of stress. The second shows visible signs of stress and the leaf was not as stiff as the healthy one. The third leaf shows severe signs of stress with little possibility of recovery. It also had a rubbery texture and was very loose. All three leaves were picked from the same plant at the same time and were all measured within an hour after they were picked. All the leaves were taped to a beam block covered in electrical tape as shown in part a). The leaves were taped down to try and make them as flat as possible so that all the changes on the FPA were due to the spectrum, not depth. The spectrometer measurements were done on the leaves while they were uncovered shown in part a). The DPC measured the leaves while they were

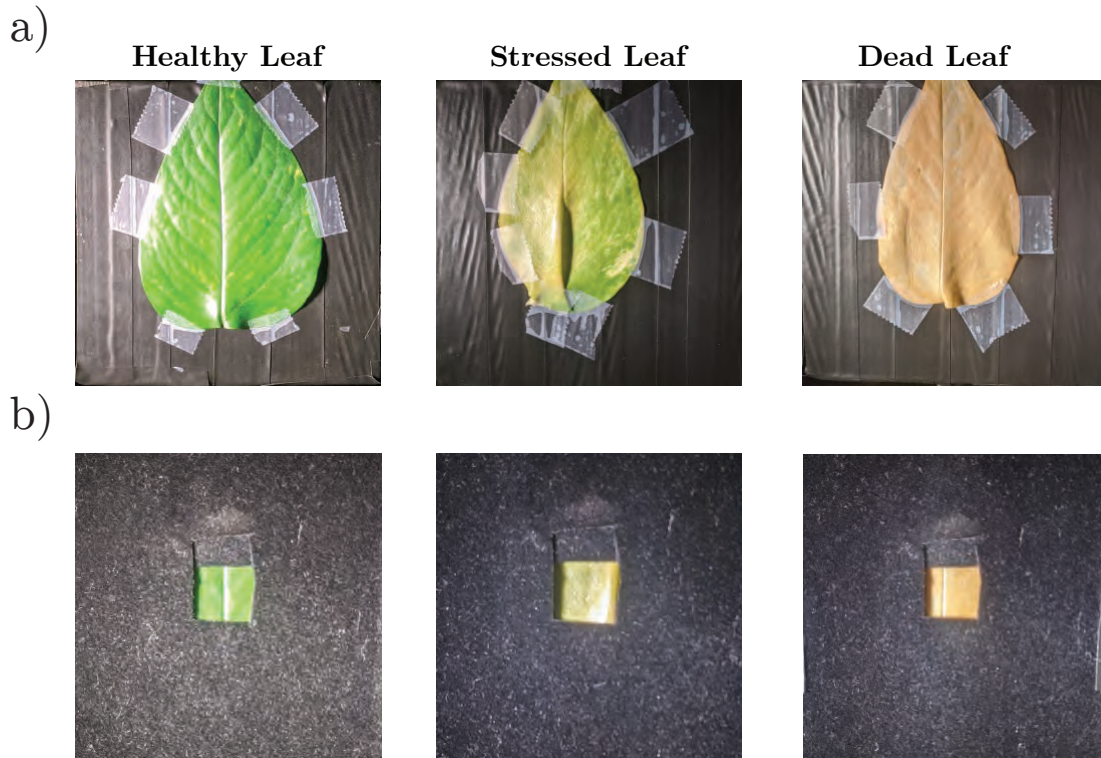
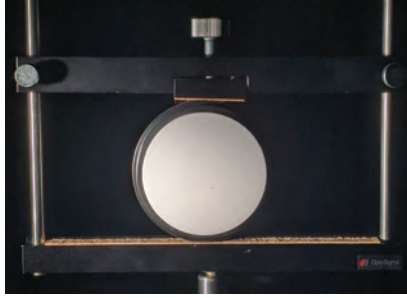


**Figure 23.** The three different scenes captured by the spectrometer and DPC for an NDVI measurement. In a), these scenes were captured by the spectrometer and contained three leaves from the same plant in decreasing health. In b), these scenes were captured by the DPC and are the same leaves as shown in part a). The black felt was placed around each leaf to minimize the noise sources.

covered with a piece of felt as shown in part b). The purpose of the felt was twofold. One, it reduces the amount of background noise contributed by the zeroth-order of diffraction by making the majority of the scene seen by the lenslets, lower. Secondly, it allows the spectrum of the leaf to extend to multiple lenslets on a target that has little reflectance. The integration time for all the scenes was kept at 1/60 second and was kept below saturation. The images of the reflectance standard captured by the grating spectrometer and DPC are displayed in Figure 24. Measurements made with the grating spectrometer included a dark current subtraction. Measurements made with the DPC included a background subtraction. The background subtraction is

done by subtracting the entire scene by the digital number collected from the felt of the raw output from the sensor. Therefore wherever there was felt, the digital number should be zero. The background subtraction resulted in the reduction of digital numbers for the signal, but in the end it boosted the NDVI collected.

a)



b)



**Figure 24.** Spectralon<sup>®</sup> source to diffusely reflect the light from the lamp. a) This scene was used to capture the source spectra from the lamp with the spectrometer. b) Black felt was placed over the Lambertian source to reduce the noise sources in the DPC. A shadow does appear in the image as the felt is not flat against the Spectralon<sup>®</sup> source.

## V. Results and Analysis

This chapter goes over the experimental results from the spectral resolution and reflectance measurements. The spectral resolution gives insight on how well the refocusing algorithm can take a planar wave and focus it down to one point. Additionally, it can provide information on how far the algorithm needs to refocus in order to defocus a point. The reflectance measurement and NDVI calculation give information on how well the DPC can handle a multi-spectral scene and how noise sources like the spectral cross-talk play a role in the system.

### 5.1 Spectral Resolution Performance

The experimental results for refocusing monochromatic light over the entire spectral range is displayed in Figure 25. A 3 x 3 square was placed at the location of the highest pixel value in all of the refocused images of a single monochromatic light and integrated for each refocused image. The refocused images that contain the highest pixel value or peak pixel value for each monochromatic light is displayed in Figure 26.

In Figure 25, it shows that as the DPC begins to image different monochromatic point sources and refocus to that wavelength, the peak irradiance drops the further it is from design. The drop in irradiance has also been seen in Shepard's dissertation in which he looked at multiple refocusing algorithms through simulation [14]. Additionally in this figure, some areas contain a constant amount of integrated irradiance, sudden drops, and blocky curves. These artifacts are due to the integer shifts within the sub-aperture images (I.E. not interpolated to receive less than one sub-aperture pixel shift) and integration of a square instead of a single pixel.

Now looking specifically at the individual curves, the design wavelength achieves

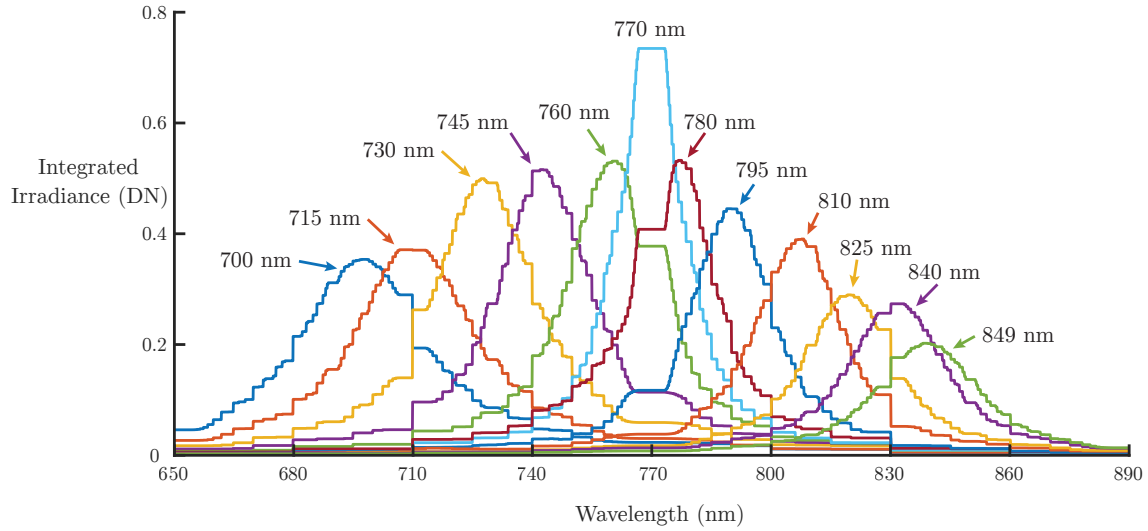


**Figure 25.** This plot was made by imaging collimated light from a tunable Ti:Sapphire laser. The laser was tuned to the labeled wavelengths on each different colored plot and the amount of optical power for each wavelength was kept constant. To make the curves, the image of the incident wavelength was refocused to all values within its spectral range. The peak pixel value was found in the refocused stack and integrated along with the immediate pixels surrounding it, making a  $3 \times 3$  square shown in Figure 21. This integration occurs at the same spatial position for every refocused image in the stack. This plot displays how the irradiance of a set group of pixels of a particular wavelength changes as it is refocused over the spectral range. The digital numbers for each pixel were normalized to a value of one.

**Table 5.** Full width half max of integrated values from the refocused images.

$\lambda$ (nm)	700	715	730	745	760	770	780	795	810	825	840	849
FWHM (nm)	35.4	35.2	32.8	28.9	29.2	20	23.5	24.4	26.8	24.1	28.4	29.3

a peak near  $770 \pm 3.3$  nm with a full width half max (FWHM) of 20 nm displayed in Table 5. As expected, the design wavelength performs the best in terms of image formation, accuracy, and broadening. As the shorter wavelengths begin to enter the DPC, the peak integrated irradiance begins to decrease despite being within the spectral range. The location at which each point source achieves its peak integrated irradiance during the refocusing process is also gradually placed further from the actual point source. For example, for a point source at 760 nm it achieves a maximum near  $760.7 \pm 0.7$  nm, while at 700 nm it achieves a maximum near  $697.8 \pm 0.8$  nm.

The shorter wavelengths also sustain much broader curves than the design wavelength. This means as the refocusing algorithm goes further from the design wavelength, the sub-aperture images will gradually come to a point for the correct wavelength and then gradually shift off the point. Ideally, the sub-aperture images would come to a point much quicker and then disperse like the design wavelength.

For wavelengths longer than design, they show the same decrease in peak integrated irradiance but with values generally lower than the shorter wavelengths. A reason for the lower peaks could be due to the spectral response of the detector. According to the camera's manufacturer, the sensor has a relative response of 0.7 near 700 nm and linearly decreases until it has a relative response of 0.4 near 850 nm. The accuracy of the longer wavelengths tended to be worse as well. For a point source at 780 nm it reached a peak at  $776.3 \pm 0.8$  nm while for a point source at 849 nm it reached a peak at  $838.7 \pm 0.6$  nm. Lastly, the longer wavelengths are broader than the design wavelength but were consistently more narrow than the shorter wavelengths.

Figure 26 best explains the decrease in peak irradiance for point sources that have a wavelength other than design. This figure displays the refocused image where the point source achieves the peak integrated irradiance value in Figure 25. Ideally, the refocused images in Figure 26 should be a single pixel like in a). However, it seems that as the point sources go further from the design wavelength, the refocusing algorithm is unable to bring it entirely down to a single pixel and creates a blur instead. One cause for this blur is due to optical aberrations which will be talked about more extensively in the next section. Another cause that may not be as significant is because wavelengths other than design will illuminate more lenslets and therefore encounter more edges. The rays that encounter the edges of the lenslet will not refract properly and end up on the outside of the lenslet image.

To get the spectral resolution of the integrated irradiance, the different curves

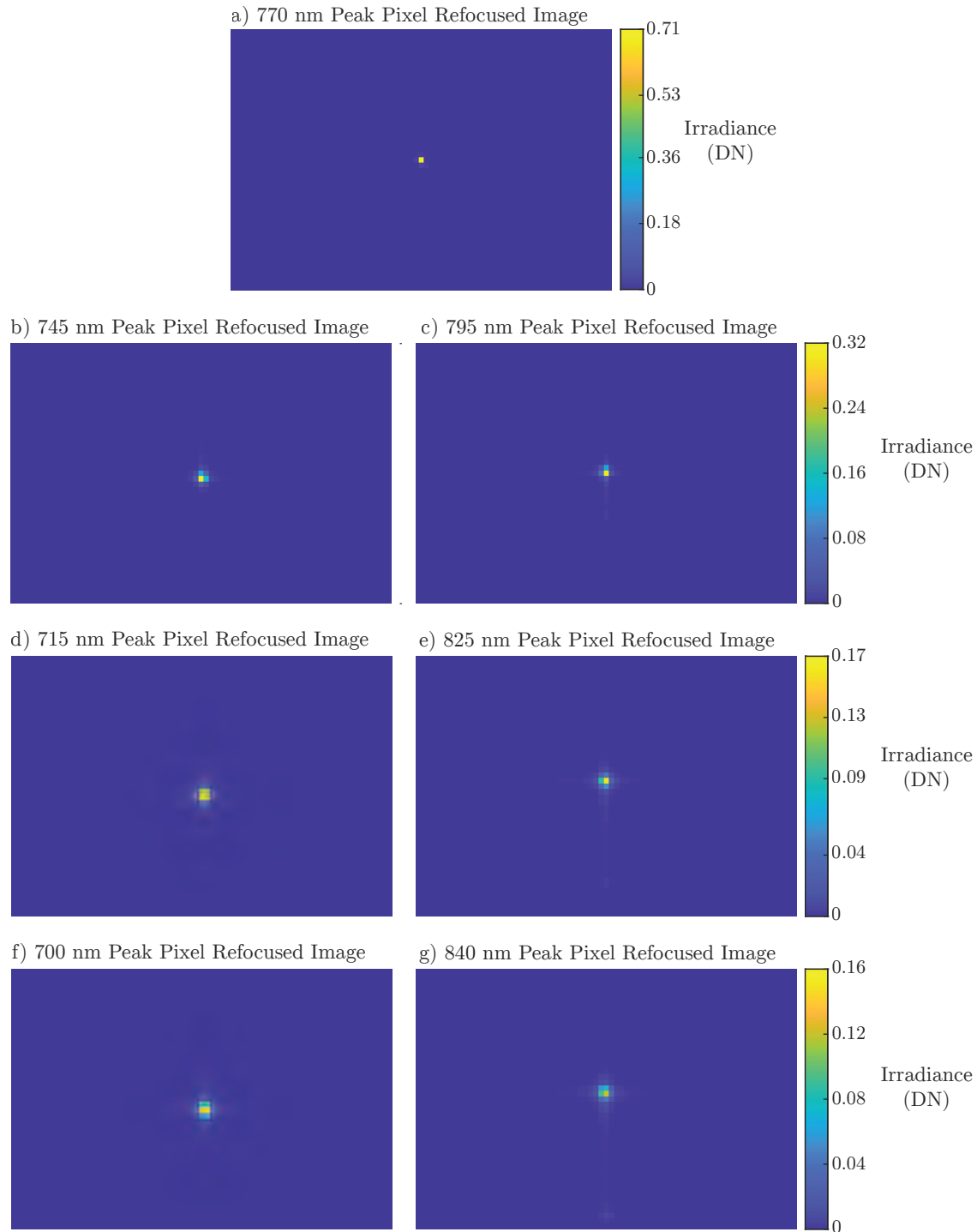


Figure 26. Each picture displays the refocused image for the peak integrated irradiance values for the corresponding point sources shown in Figure 25. a) shows the point source with the design wavelength while the left column shows point sources with wavelengths shorter than design and the right column shows longer wavelengths. Each row is set up to have point sources that have wavelengths equally as far away from the design wavelength. The units for each pixel is a normalized digital number that has a maximum of 1 and a minimum of 0. Each refocused image should be a single pixel like in a), but the refocusing algorithm is unable to bring the pixels back to a single point.

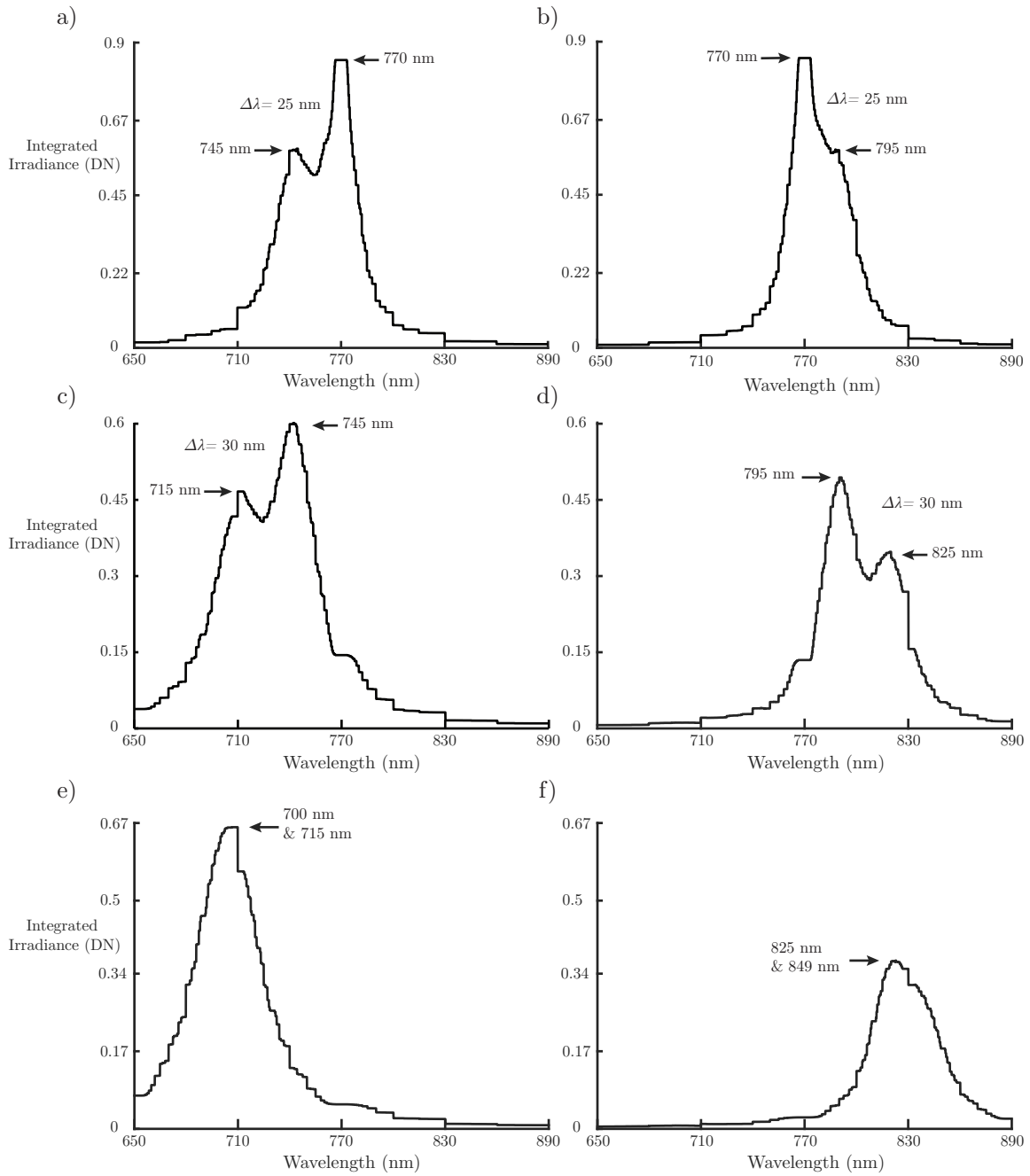


Figure 27. To conduct the spectral resolution, the curves for each point source in Figure 25 are added together and considered resolved using the Sparrow criterion. Point sources that have wavelengths shorter than design are placed in the left column and the longer than design point sources are placed on the right. Graphs a) - d) display point sources that just meet or substantially exceed Sparrow's criterion while graphs e) and f) show point sources that are not considered resolvable. All graphs exceed the predicted spectral resolution of 6.06 nm.

for each point source from Figure 25 are added together and are considered resolved by the Sparrow's criterion. The left column are point sources that had wavelengths shorter than design, while the right side was longer than design. It is immediately evident that the predicted spectral resolution of  $\Delta\lambda = 6.06$  nm is not sufficient enough to consider two point sources of different wavelengths resolved. The point sources that were shown in Figure 25 but not shown in Figure 27 were tested but did not meet the criterion like graphs e) and f). Graphs a) and b) both show that the DPC can resolve wavelengths that are 25 nm apart on either side of the design wavelength. However, a) dramatically exceeds the Sparrow criterion and can most likely resolve wavelengths 20 nm apart. On the other hand, b) only slightly exceeds the criterion and may only resolve wavelengths 24 nm apart. Graphs c) and d) both show that the DPC can resolve wavelengths that are 30 nm apart though they are 25 nm from the design wavelength. Both graphs greatly exceed the criterion but will most likely be able to resolve wavelengths that are 25 nm apart. Graph f) was included to show that even though the DPC was able to detect wavelengths 25 nm apart near the design wavelength, it is unable to hold this separation the further from design the wavelengths become.

Overall, the refocusing algorithm plays a large part in determining the spectral resolution of the DPC. Figure 26 shows that as the point source strays away from the design wavelength, the refocusing algorithm will create a larger blur for the peak irradiance value. As a result of this blur, the integrated irradiance will have a lower peak value the further it is from design as shown in Figure 25. This figure also shows that for far away wavelengths, they encounter a more substantial broadening compared to the wavelengths closer to the design. Lastly, due to the broadening of the refocusing algorithm alone, this will increase the spectral resolution from the predicted value. The spectral resolution of the DPC will increase the further from the

design the wavelengths become and are more than likely not equal for wavelengths on either side of the design wavelength.

## 5.2 NDVI & Multi-Spectral Performance

The measured spectra of the three leaves with the grating spectrometer were shown to agree with the results found in other studies [28] [36]. As shown in Figure 28, the red edge becomes further blue-shifted as the leaf begins to die. The shift is caused by the degradation of the chlorophyll which leaves behind the spectral characteristics of the carotenes and xanthophylls, which degrade slower. For the stressed leaf specifically, the increase in the 500 - 700 nm range gives the leaf its yellowish-greenish colors shown in Figure 23. For the dead leaf, the decrease in reflectance in the NIR is most likely due to the development of tannins which are the brown pigments in the leaf. However, the spectral structure seems to show that most of the chlorophyll has died, but the xanthophylls are still present within the leaf which gives it a constant reflectance from 550 - 700 nm. Now that the spectra of all three leaves are known, the NDVIs can be calculated with error propagated due to the thermal drift of the FPA. The healthy leaf had an NDVI of  $0.860 \pm 0.034$ , the stressed leaf had a value of  $0.380 \pm 0.031$ , and the dead leaf had a value of  $0.032 \pm 0.034$ .

With the spectra and NDVI values known for each leaf, they can be compared to the values found by the DPC. The raw refocused data are shown in Figure 29 displays the three different leaves refocused to 660, 770, and 860 nm. For all of them, they show the phenomena in the previous section in which the design wavelength displays the highest value even though light at 860 nm should have the same amount of signal. Additionally, the 770 nm refocused data is generally sharper with less blur near its edges. Generally, for the 660 nm refocused images, there seems to be a large gathering of blue near the bottom of the image which is not expected. A similar effect

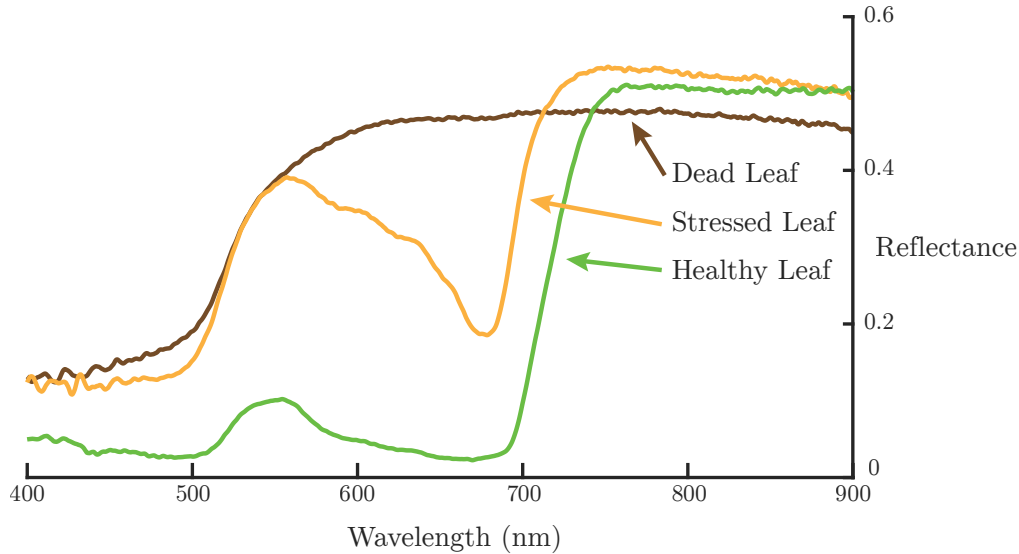
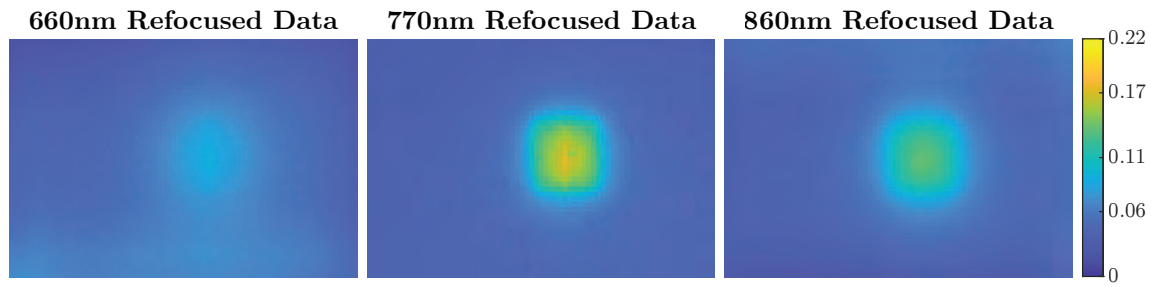


**Figure 28.** Reflectance measurements from the grating spectrometer of the three different leaves. The healthy leaf displayed expected values for vegetation with a small increase near 550 nm and a sharp red edge near 700 nm. For the stressed leaf measurement, parts of the leaf begin to degrade which leads to an overall increase in the reflectance in the visible and gives the leaf a yellowish-greenish appearance. For the dead leaf measurement, most of the chlorophyll has died which gives a high constant reflectance until 550 nm in which absorption by the xanthophyll appears.

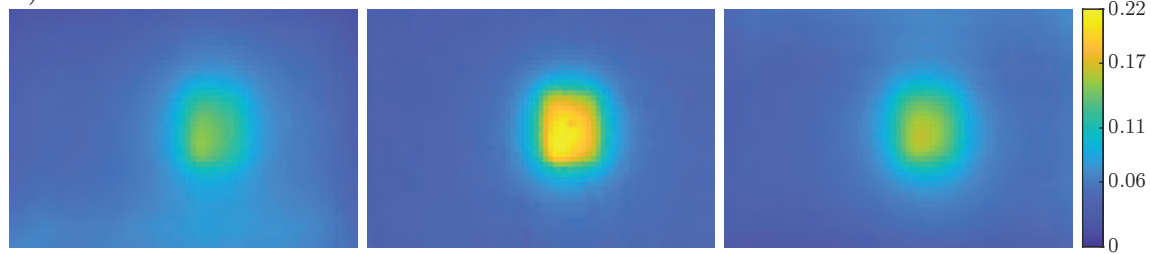
can be seen on the top of the images for the 860 nm images.

The reflectance data is shown in Figure 30, which displays the same images as in Figure 29 but is calibrated to the Spectralon<sup>®</sup> standard refocused to the same wavelengths. In a) the reflectance matches the correct modulation for a healthy leaf: a high reflectance near 860 nm and a low reflectance near 660 nm. The actual value for the reflectance of the leaf in comparison to the spectrometer measurement is higher than what is expected. The values shown here were averaged over the location of the square and the standard error was taken. The uncertainty represents the statistical variation on the area of the leaf. At 860 nm, the DPC displays values of approximately  $0.643 \pm 0.004$  while the spectrometer measured about  $0.527 \pm 0.034$ . At 660 nm, the DPC displayed values of  $0.400 \pm 0.002$  while the spectrometer read the measurement of  $0.040 \pm 0.010$ . The cause of the inflation of both of these values is most likely

a) Healthy Leaf



b) Stressed Leaf



c) Dead Leaf

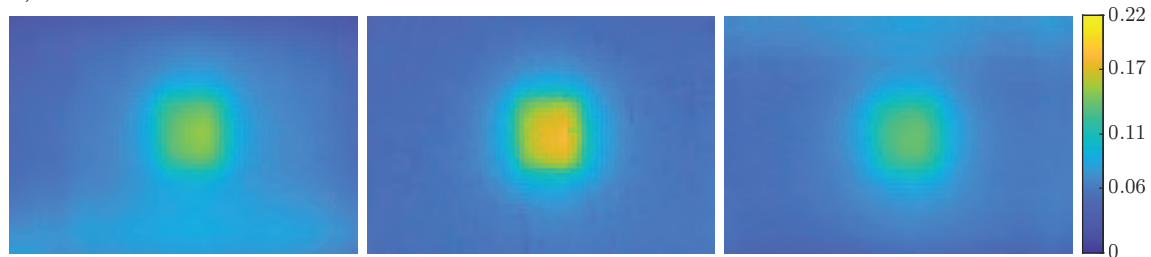
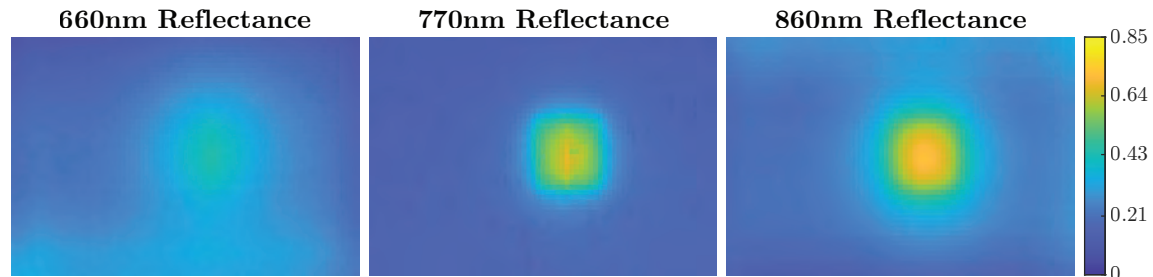


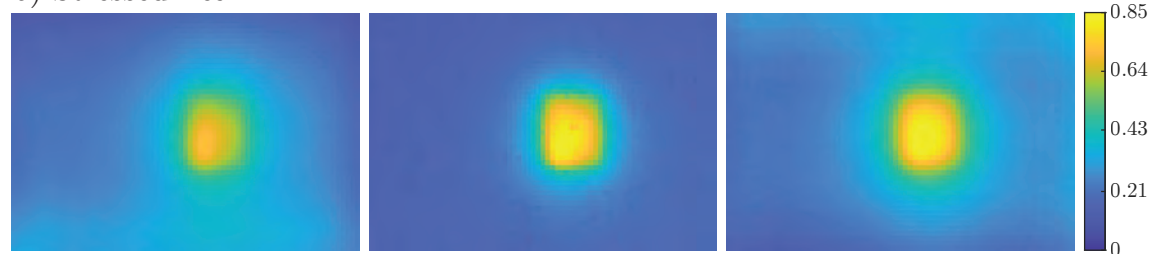
**Figure 29.** Each row displays a background-subtracted scene containing one of the leaves while each column displays the refocused image of the corresponding wavelength. The values outputted are units of digital numbers. a) The scene contains the image of a healthy leaf. The data seems to show there is a noticeable difference between the 860 and 660 nm refocused images. b) The scene contains the image of a stressed leaf. Here the difference between the two refocused images seems slim but the 860 nm image appears to be slightly higher. c) The scene contains the image of a dead leaf. The difference between the two refocused images looks to show that the 660 nm has higher values than 860 nm. Both refocused images also contain a considerable amount of noise outside the square.

due to spectral contamination from the spectral-spatial overlay. Since the leaf had a strong response in its reflectance from 755 – 900 nm, it contaminated pixels where the leaf was and the refocusing algorithm gave the 660 nm image higher values. In b) it shows that the reflectance of the leaf at 860 nm is still higher than 660 nm. However, the 660 nm refocused image does show an increase in reflectance from a).

a) Healthy Leaf



b) Stressed Leaf



c) Dead Leaf

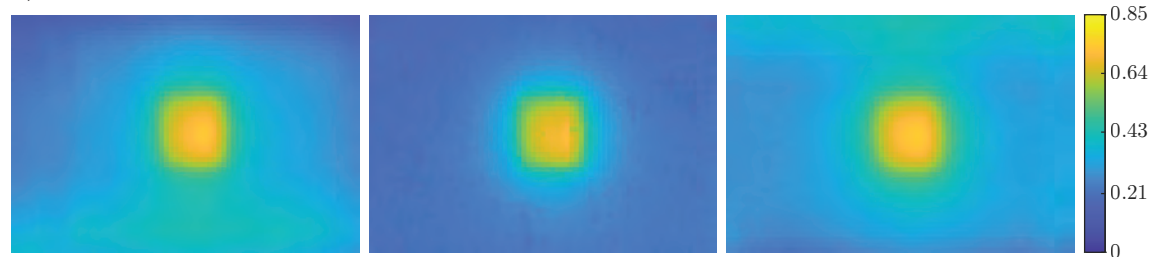


Figure 30. Each row displays a background-subtracted scene containing one of the leaves while each column displays the refocused image of the corresponding wavelength. The values displayed on the images are in terms of reflectance. a) The scene contains the image of a healthy leaf. Here the leaf displays an expected high value at 860 nm and a lower value at 660 nm. Additionally, there are larger amounts of noise near the top or bottom of the refocused image. b) The scene contains the image of a stressed leaf. It is expected that the values are similar to a) but since the leaf is stressed, it should have a more substantial reflectance at 660 nm in which it displays. The amount of noise at the top and bottom is similar to the healthy leaf. c) The scene contains the image of a dead leaf. Here the values are the same for all three refocused images, which is what is expected given figure 28. The noise here is substantially higher than the previous two leaves.

This is good news as the DPC is able to collect higher and lower wavelengths from the design wavelength despite the artifacts. Lastly, in c) it shows that in all three refocused images the leaf has about the same reflectance. This is again good news as the spectrometer also confirms that the spectrum is indeed the same across the wavelengths. The spatial detail for all three leaves does show where the location of the square is. Towards the edges of the box there does seem to be the softening of edges, particularly for refocused images other than design. However, the biggest concern is the large artifacts created in areas that are not the leaf, which was previously mentioned the raw refocused images. The artifacts can cause false positives in the NDVI for areas of no vegetation or false negatives for areas that do contain vegetation.

The NDVI measurement of the scenes is given in Figure 31. In all three images, the DPC can determine the location of the leaf and provide positive NDVI values for spectra that follow the modulation in the two bands. The NDVI's were calculated from the averaged reflectance values and the errors were propagated through. The healthy leaf displays an NDVI value near  $0.233 \pm 0.004$  which is considerably lower than the spectrometer's value of 0.860. The decrease can be attributed to the high reflectance value in the 660 nm refocused image or to artifacts added to both bands. The stressed leaf displays an NDVI value near  $0.093 \pm 0.005$ , which can be attributed to the same reason. Lastly, the NDVI for the dead leaf shows a value of  $0.009 \pm 0.004$  which is within the error of what the spectrometer measured.

As mentioned previously, artifacts created in the refocused images off of the design wavelength caused false positives and surprisingly large negative areas. One of the major causes of the false values is due to the optical aberrations that are present within the DPC. Figure 32 displays the sub-aperture view of the Spectralon<sup>®</sup> sample with zoomed-in pictures of the individual sub-aperture images. Each sub-aperture image should be an image of a square as shown in Figure 24 and Figure 20 part b).

However, as the sub-aperture images become further from the central sub-aperture, the images become skewed. This is a result of the FPA imaging an aberrated light field. In a realistic system, the images of the lenslets are not directly behind them; instead they become off-center the further they are from the FZP's optical axis as shown in Figure 33 diagram a). The subsequent sub-aperture image is done by taking the same pixel location behind each image made by the MLA. In b), the rays that make up each sub-aperture image have different optical path lengths which are not symmetric about its optical axis unless it is aligned with the FPZ's optical axis. To point out any one aberration within the DPC is difficult as the intersection of rays with the aperture of the system increases away from the optic axis, problems like spherical aberration, coma, astigmatism, field curvature, and distortion increases to varying degrees. Additionally, these aberrations can also be a function of object distance or angle it makes with the lens. Regardless of the aberrations present in the sub-aperture images, they do explain the increase in digital numbers in areas that are not the square in Figure 29. As the refocusing algorithm shifts the aberrated sub-aperture images, the problem worsened because the aberrated values are now able to

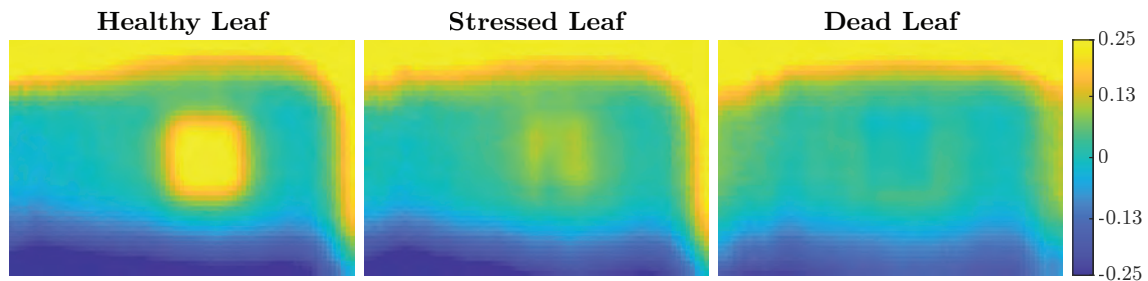


Figure 31. By using the reflectance measurements show in Figure 30, the NDVI is calculated for each pixel on the scene. The healthy and stressed leaf both show positive values for the NDVI but at reduced values in comparison to the grating spectrometer. The dead leaf displays an NDVI of 0 in all areas within the square which is in agreement with the spectrometer value. There are also false positives and negatives near the edges of the refocused image contributed by the noise described in the reflectance measurements.

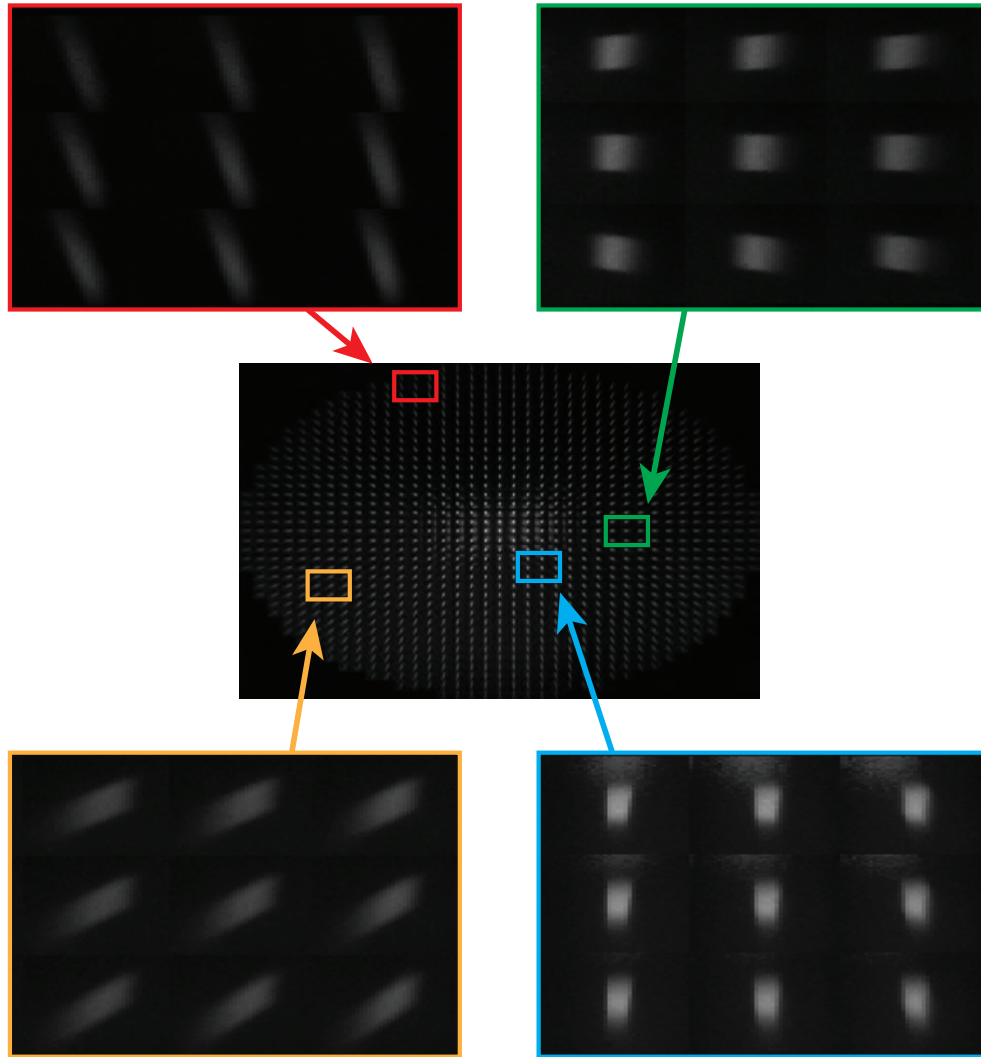


Figure 32. The center image displays the sub-aperture view of the Spectralon<sup>®</sup> sample, which is the same image as in Figure 20. Each colored box is a magnified picture within the sub-aperture view to show the individual sub-aperture images at their respective  $(u, v)$  locations. Each sub-aperture image should be a square but as the angular coordinates go further from the center, the more aberrated the sub-aperture images become.

reach further parts of the final refocused image.

In order to fix the aberrations within the light field two methods can be done. The first would be to accurately model the system taking into account all the geometry of the optical elements and derive a sampling pattern on the FPA. The description

of how to do this is thoroughly explained in Ng's dissertation in chapter 7 [25]. The second method based on a classical technique, is to stop down the lens. This is equivalent to deleting the sub-aperture images that are further from the FZP's optic axis. To see the effect this has on the refocusing algorithm, Figure 34 shows the NDVI retaken of the same leaves but only used sub-aperture images that are at the angular coordinates  $(0 \pm 5\Delta u, 0 \pm 5\Delta v)$ . In comparison to the other NDVI values in Figure 31, the healthy leaf shows a sharper image where the square leaf is but has a decreased NDVI value. For the other leaves, stopping down the lens seemed to have little to no effect to create a sharper image. The false positives near the edges occupy a smaller amount of pixels but are still present. Areas outside the square show significant variation within the NDVI but most are zero or negative. This could be the result of the zeroth-order noise as only the central sub-apertures were used. If additional sub-apertures contributed to the final image, then the zeroth-order should have less of an effect as there are more sub-apertures to average on a single pixel.

While the stopping down the aperture of the system did reduce some of the edge

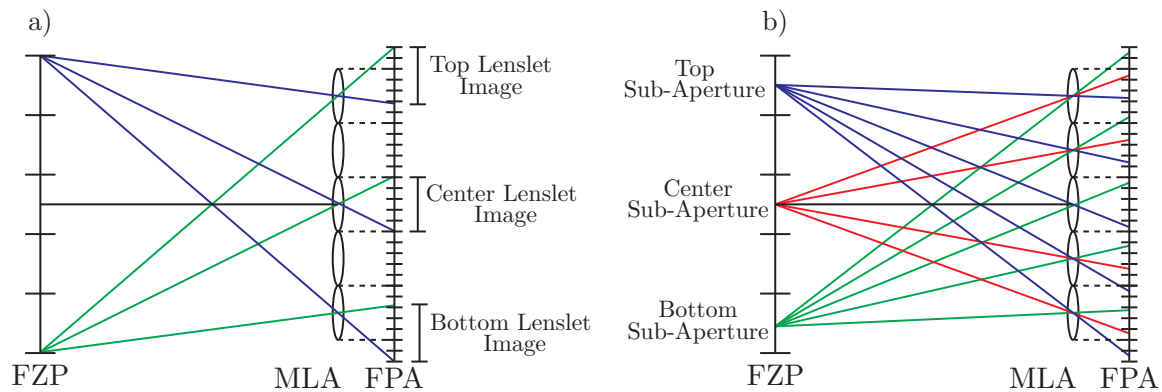


**Figure 33.** Both diagrams show how the DPC realistically collects lenslet images and sub-aperture images. a) shows the lenslet images are shifted on the FPA based on how far they are from FZP's optical axis. b) shows that optical path length traversed for each ray in a single sub-aperture image is unequal for sub-aperture images near the edges of the FZP. The optical path length differences and other factors result in aberrations for sub-aperture images far from the FZP's optical axis.

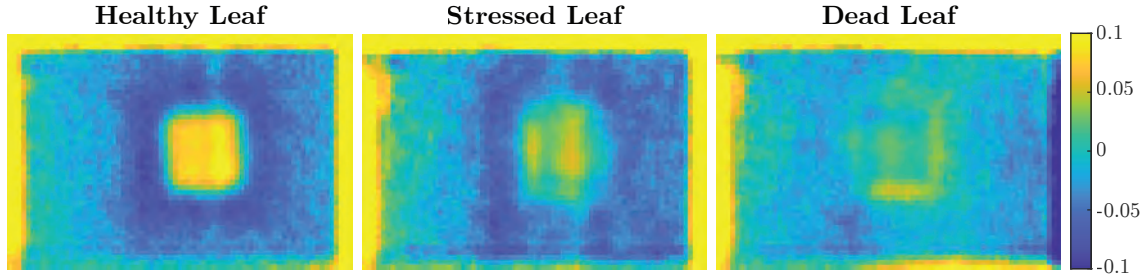


Figure 34. These measurements were taken the same way as Figure 31 but the only sub-aperture images used are at the coordinates  $(0 \pm 5\Delta u, 0 \pm 5\Delta v)$ . The increased amount of noise in areas outside the square is due to the zeroth-order contribution to the central sub-aperture images.

effects and made the healthy leaf appear sharper, it would be interesting to see how the algorithm refocuses with only aberrated sub-aperture images. Figure 35 removes the sub-aperture images with the angular coordinates of  $(0 \pm 9\Delta u, 0 \pm 9\Delta v)$ , leaving behind only the severely aberrated images. All three NDVI's show a similar picture to the original measurement in Figure 31. The false positives and negatives have grown near the edges and attain higher values. The healthy leaf now has more of a circular blur to it than the square shape and has much higher values than the original NDVI. The dead leaf shows a surprisingly sharp image of where the square is with little artifact near the center of the image.

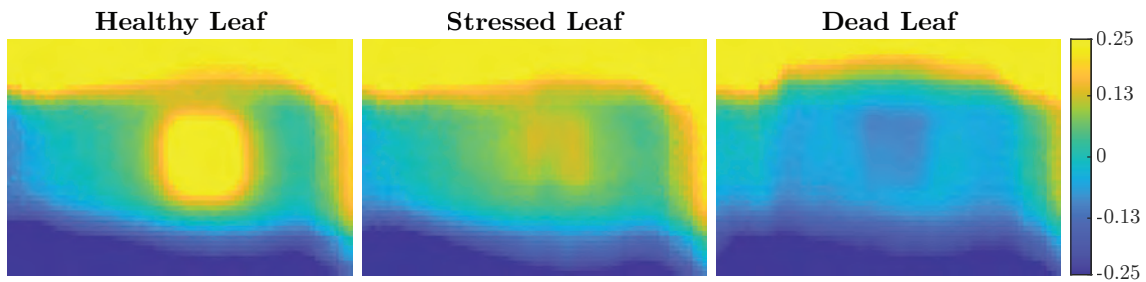


Figure 35. These measurements were taken the same way as Figure 31 but the sub-aperture images at the coordinates  $(0 \pm 9\Delta u, 0 \pm 9\Delta v)$  are removed. This leaves only the aberrated sub-apertures to shift and add together to create the final refocused images.

## VI. Conclusion

### 6.1 Contributions

This study demonstrated that the DPC can be used as a multi-spectral imager to calculate an NDVI. Design equations were developed to tie the system parameters to the camera's multi-spectral performance, which were used to design and build a DPC to look at NDVI. Next, sources of artifacts such as the zeroth-order of diffraction and the spatial-spectral overlay were identified and accounted for during the experiment. The first experiment demonstrated the refocusing algorithm's ability to take incoming point sources of varying wavelengths and refocus the images back down to one point. From here, the spectral resolution was tested based on the Sparrow criterion. The second experiment demonstrated that the DPC can detect differences in the spectral composition of the scene despite the artifacts unique to the system.

The experimental results yielded information about the performance of the DPC. The spectral resolution of the system did not meet the expected value of 6.06 nm from the design equation. For wavelengths shorter than design, the resolution was found to be 25 nm while for longer wavelengths, the resolution was 30 nm. A major contributor for the increase in spectral resolution is the spread of spectral irradiance values the further the system refocused. The NDVI measurement was successful in getting positive values for the location of the leaf, however the NDVI values were not as large as those measured by the spectrometer. The cause of the reduced values is due to energy leaking into nearby refocused images at other wavelengths. Additionally, optical aberrations within the DPC caused false positives and negatives to occur near the edges of the FOV.

## 6.2 Future Work

This is the first time the DPC has been demonstrated to work experimentally on a multi-spectral scene. Future work should focus on reducing the amount of background noise discussed in section 3.2, reducing optical aberrations, and the refocusing algorithm it-self. One way to reduce the amount of background noise contributed from the zeroth-diffraction order or increase the diffraction efficiency of the first order is to change the design of the diffractive optic. One diffractive optic design that should be considered is the Rayleigh-Wood phase-reversal zone plate which increases the diffraction efficiency of the first order to  $\frac{4}{\pi^2}$  and eliminates the zeroth-order of diffraction [37]. However, the odd higher orders receive an increase in diffraction efficiency as well. Another way to reduce the zeroth-order of diffraction is to reconfigure to what is called the intermediate image diffractive plenoptic camera (IIDPC) [38]. This system is based on the focused plenoptic camera design by Lumsdaine in which the MLA is placed some distance  $a$  away from the design focus of the system. As a result, the FPA is placed a distance  $b$  that is in accordance with the thin lens equation 14. Images can be refocused after image capture but with a different refocusing algorithm and receive an increase in spatial sampling at the cost of lower angular sampling. The IIDPC replaces the primary optic with a diffractive one similar to the DPC and again the changes are due to spectral variation and not depth as shown in Figure 36. The idea here is that because the FPA is placed away from the focus of the MLA, the zeroth-order will contribute less background noise to the system. Additionally, according to the work of Diaz, if the distance is picked such that  $a = b$ , the spatial resolution will be a maximum [39]. When this occurs the MLA system becomes a  $2f$  imaging system and allows the zeroth order to become a uniform blur behind each lenslet as shown in Figure 36.

To reduce the background noise from the spatial-spectral overlay, the most nat-

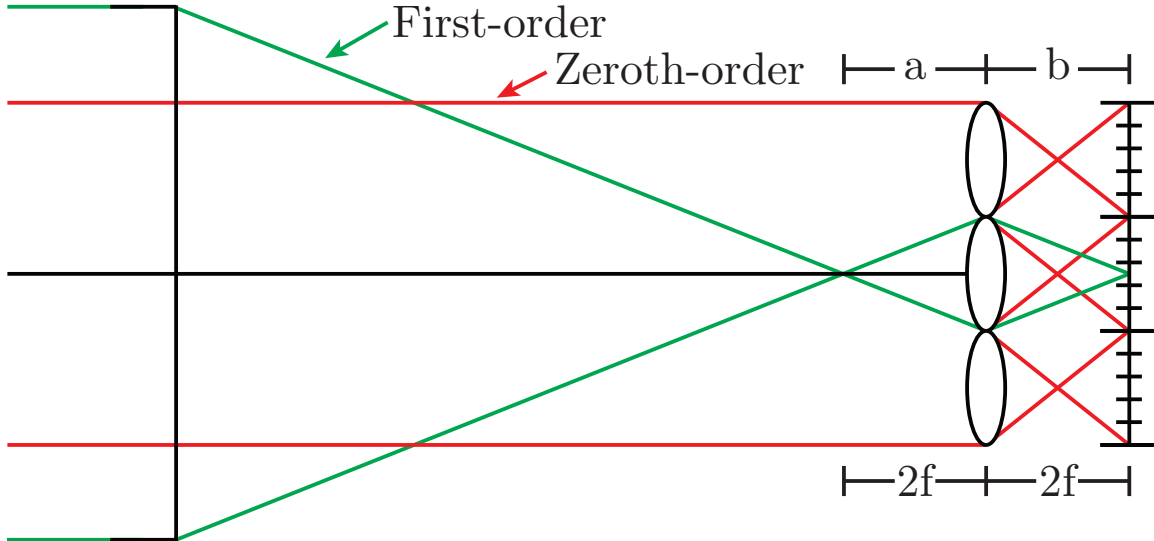


Figure 36. This figure displays another proposed system to digitally refocus wavelengths based on the focused plenoptic camera design [13]. The image plane is now placed some distance  $a$  away from the MLA and the FPA is placed at some distance  $b$  in accordance with the thin lens equation. For this particular setup, it is maximized for best spatial resolution where  $a$  and  $b$  are equal to each other, which is twice the lenslet focal length. The  $2f$  spacing is advantageous as the zeroth-order becomes a uniform blur on the FPA.

ural solution would be to use notch filters. In the DPC's current setup, it accepts wavelengths starting from the lowpass filter of 650 nm, all the way to the end of the sensor's response at 1000 nm. If the only bands needed are near 660 nm and 860 nm, then all other bands are contributing background noise to the refocused images. Therefore placing a notch filter at wavelengths of interest should be useful in cutting down the spatial-spectral overlay.

To correct the optical aberrations within the DPC, the first step would be to do a rigorous analysis of the different types of aberrations present. Afterward, an optical system including the diffractive optic can be designed to reduce the aberrations that are imaged onto the FPA. Another method that was briefly mentioned in section 5.2 is to model the DPC in order to create a digital correction algorithm. The model would be able to derive an aberrated sampling grid onto the FPA so that the algorithm will collect the correct pixels for refocusing.

The last type of noise that can be reduced is the noise generated by the refocusing algorithm itself. One method that shows promise in increasing the spectral resolution and cleaning up the refocused image is to perform 3-D deconvolution techniques. This technique can take into account the point spread function (PSF) that occurs on the sensor when wavelengths other than design are incident on the system. The 3D deconvolution should be able to deconvolve the raw sensor image to the specific wavelength and can be sent through the refocusing algorithm. However, this method requires careful measurement of different wavelength's PSF.

## Bibliography

1. J. Berni, P. Zarco-Tejada, L. Suárez, V. González-Dugo, and E. Fereres, “Remote sensing of vegetation from UAV platforms using lightweight multispectral and thermal imaging sensors,” *Int. Arch. Photogramm. Remote Sens. Spatial Inform. Sci.*, 2009. [Online]. Available: <https://pdfs.semanticscholar.org/3cf0/9e91bdd760a0ee22210190e1869d6e6391cd.pdf>
2. P.-J. Lapray, X. Wang, J.-B. Thomas, and P. Gouton, “Multispectral Filter Arrays: Recent Advances and Practical Implementation,” *Sensors*, vol. 14, no. 11, pp. 21 626–21 659, nov 2014. [Online]. Available: <http://www.mdpi.com/1424-8220/14/11/21626>
3. C. J. Tucker, “Red and Photographic Infrared Linear Combinations For Monitoring Vegetation,” Greenbelt, Tech. Rep., 1978. [Online]. Available: <https://ntrs.nasa.gov/search.jsp?R=19780024582>
4. L. J. Rickard, R. W. Basedow, E. F. Zalewski, P. R. Silvergate, and M. Landers, “HYDICE: an airborne system for hyperspectral imaging,” in *Imaging Spectrometry of the Terrestrial Environment*, G. Vane, Ed., vol. 1937, no. September 1993, sep 1993, p. 173. [Online]. Available: <http://proceedings.spiedigitallibrary.org/proceeding.aspx?doi=10.1117/12.157055>
5. M. Descour and E. Dereniak, “Computed-tomography imaging spectrometer: experimental calibration and reconstruction results,” *Applied Optics*, vol. 34, no. 22, p. 4817, aug 1995. [Online]. Available: <https://www.osapublishing.org/abstract.cfm?URI=ao-34-22-4817>
6. A. Bodkin, A. Sheinis, A. Norton, J. Daly, S. Beaven, and J. Weinheimer, “Snapshot hyperspectral imaging: the hyperpixel array camera,” in *Algorithms*

and Technologies for Multispectral, Hyperspectral, and Ultraspectral Imagery XV, S. S. Shen and P. E. Lewis, Eds., vol. 7334, no. April 2009, may 2009, p. 73340H. [Online]. Available: <http://proceedings.spiedigitallibrary.org/proceeding.aspx?doi=10.1117/12.818929>

7. Z. Zhou and B. Xiangli, "Snapshot Multispectral Imaging Using a Plenoptic Camera with an Axial Dispersion Lens," in *Classical Optics 2014*. Washington, D.C.: OSA, 2014, p. CTu2C.4. [Online]. Available: <https://www.osapublishing.org/abstract.cfm?uri=COSI-2014-CTu2C.4>
8. F. D. Hallada, A. L. Franz, and M. R. Hawks, "Fresnel zone plate light field spectral imaging," *Optical Engineering*, vol. 56, no. 8, p. 081811, jul 2017. [Online]. Available: <http://opticalengineering.spiedigitallibrary.org/article.aspx?doi=10.1117/1.OE.56.8.081811>
9. R. Ng, "Fourier slice photography," *ACM Transactions on Graphics*, vol. 24, no. 3, p. 735, jul 2005. [Online]. Available: <http://portal.acm.org/citation.cfm?doid=1073204.1073256>
10. F. Hallada, "The Fresnel Zone Light Field Spectral Imager," Master's Thesis, Air Force Institute of Technology, jun 2017. [Online]. Available: <https://scholar.afit.edu/etd/786/>
11. G. Andersen, O. Asmolova, M. G. McHarg, T. Quiller, and C. Maldonado, "FalconSAT-7: a membrane space solar telescope," in *Space Telescopes and Instrumentation 2016: Optical, Infrared, and Millimeter Wave*, H. A. MacEwen, G. G. Fazio, M. Lystrup, N. Batalha, N. Siegler, and E. C. Tong, Eds., jul 2016, p. 99041P. [Online]. Available: <http://proceedings.spiedigitallibrary.org/proceeding.aspx?doi=10.1117/12.2229711>

12. C. Diaz, "Spatial Resolution and Contrast of a Focused Diffractive Plenoptic Camera," Master's Thesis, Air Force Institute of Technology, 2018. [Online]. Available: <https://scholar.afit.edu/etd/1745/>
13. A. Lumsdaine and T. Georgiev, "The focused plenoptic camera," in *2009 IEEE International Conference on Computational Photography (ICCP)*. IEEE, apr 2009, pp. 1–8. [Online]. Available: <http://ieeexplore.ieee.org/document/5559008/>
14. J. Shepherd, "Evaluation and Quantification of Diffractive Plenoptic Camera Algorithm Performance," Ph.D. dissertation, Air Force Institute of Technology, 2015. [Online]. Available: <https://scholar.afit.edu/etd/1954>
15. A. Vijayakumar and S. Bhattacharya, *Design and Fabrication of Diffractive Optical Elements with MATLAB*, 1st ed. SPIE, jan 2017. [Online]. Available: <https://spiedigitallibrary.org/ebooks/TT/Design-and-Fabrication-of-Diffractive-Optical-Elements-with-MATLAB/eISBN-9781510607064/10.1117/3.2261461>
16. D. Attwood, "Soft X-Ray Microscopy with Diffractive Optics," in *Soft X-Rays and Extreme Ultraviolet Radiation*, 1st ed. Cambridge University Press, aug 1999, ch. 9, pp. 337–394. [Online]. Available: <https://www.cambridge.org/core/product/identifier/CBO9781139164429A085/type/book{-}part>
17. Y. Suzuki, A. Takeuchi, H. Takenaka, and I. Okada, "Fabrication and Performance Test of Fresnel Zone Plate with 35 nm Outermost Zone Width in Hard X-Ray Region," *X-Ray Optics and Instrumentation*, vol. 2010, pp. 1–6, 2010. [Online]. Available: <http://www.hindawi.com/archive/2010/824387/>

18. M. Sussman, "Elementary Diffraction Theory of Zone Plates," *American Journal of Physics*, vol. 28, no. 4, pp. 394–398, apr 1960. [Online]. Available: <http://aapt.scitation.org/doi/10.1119/1.1935811>
19. O. E. Myers, "Studies of Transmission Zone Plates," *American Journal of Physics*, vol. 19, no. 6, pp. 359–365, sep 1951. [Online]. Available: <http://aapt.scitation.org/doi/10.1119/1.1932827>
20. F. L. Pedrotti, L. S. Pedrotti, and L. M. Pedrotti, *Introducion To Optics*, 3rd ed. Pearson, 2006.
21. J. A. Cox, T. R. Werner, J. C. Lee, S. A. Nelson, B. S. Fritz, and J. W. Bergstrom, "Diffraction efficiency of binary optical elements," in *Computer and Optically Formed Holographic Optics*, I. Cindrich and S. H. Lee, Eds., vol. 1211, no. May 1990, may 1990, p. 116. [Online]. Available: <http://proceedings.spiedigitallibrary.org/proceeding.aspx?doi=10.1117/12.17953>
22. E. H. Adelson and J. R. Bergen, "The Plenoptic Function and the Elements of Early Vision," in *Computational Models of Visual Processing*. The MIT Press, 1991, pp. 3–20. [Online]. Available: <https://direct.mit.edu/books/book/4264/chapter/179288>
23. E. Adelson and J. Wang, "Single lens stereo with a plenoptic camera," *IEEE Transactions on Pattern Analysis and Machine Intelligence*, vol. 14, no. 2, pp. 99–106, 1992. [Online]. Available: <http://ieeexplore.ieee.org/document/121783/>
24. R. Ng, M. Levoy, M. Bredif, G. Duval, M. Horowitz, and P. Hanrahan, "Light Field Photography with a Hand-held Plenoptic Camera," Stanford University, Tech. Rep., 2005. [Online]. Available: <http://www2.ene.unb.br/mylene/PI/refs/lfcamera-150dpi.pdf>

25. R. Ng, "Digital light field photography," Ph.D. dissertation, Stanford University, 2006. [Online]. Available: <https://www.lytro.com/renng-thesis.pdf> [http://testcis.cis.rit.edu/~cnspci/references/dip/light\\_field\\_photography/ng2006.pdf](http://testcis.cis.rit.edu/~cnspci/references/dip/light_field_photography/ng2006.pdf)
26. G. Karp, *Cell and Molecular Biology: Concepts and Experiments*, 6th ed. Hoboken, NJ: Wiley & Sons, 2009.
27. D. Sadava, M. Berenbaum, C. Heller, and D. Hillis, *Life: The Science of Biology*, 9th ed. New York, NY: W.H. Freeman, 2009.
28. M. T. Eismann, *Hyperspectral Remote Sensing*, 1st ed. SPIE, apr 2012. [Online]. Available: <https://spiedigitallibrary.org/ebooks/PM/Hyperspectral-Remote-Sensing/eISBN-9780819487889/10.1117/3.899758>
29. H. Z. Mohd Shafr, M. A. Mohd Sall, and A. Ghiyamat, "Hyperspectral Remote Sensing of Vegetation Using Red Edge Position Techniques," *American Journal of Applied Sciences*, vol. 3, no. 6, pp. 1864–1871, jun 2006. [Online]. Available: <http://www.thescipub.com/abstract/?doi=ajassp.2006.1864.1871>
30. L. Kumar, K. Schmidt, S. Dury, and A. Skidmore, "Imaging Spectrometry and Vegetation Science," in *Imaging Spectrometry*. Dordrecht: Kluwer Academic Publishers, 2006, pp. 111–155. [Online]. Available: [http://www.springerlink.com/index/10.1007/0-306-47578-2\\_5](http://www.springerlink.com/index/10.1007/0-306-47578-2_5)
31. Y. Kaufman and D. Tanre, "Atmospherically resistant vegetation index (ARVI) for EOS-MODIS," *IEEE Transactions on Geoscience and Remote Sensing*, vol. 30, no. 2, pp. 261–270, mar 1992. [Online]. Available: <http://ieeexplore.ieee.org/document/134076/>

32. A. Huete, "A soil-adjusted vegetation index (SAVI)," *Remote Sensing of Environment*, vol. 25, no. 3, pp. 295–309, aug 1988. [Online]. Available: <https://linkinghub.elsevier.com/retrieve/pii/003442578890106X>
33. T. Atherton and D. Kerbyson, "Size invariant circle detection," *Image and Vision Computing*, vol. 17, no. 11, pp. 795–803, sep 1999. [Online]. Available: <https://linkinghub.elsevier.com/retrieve/pii/S0262885698001607>
34. J. Bolan, E. Hall, C. Clifford, and B. Thurow, "Light-Field Imaging Toolkit," *SoftwareX*, vol. 5, pp. 101–106, 2016. [Online]. Available: <https://linkinghub.elsevier.com/retrieve/pii/S2352711016300127>
35. C. M. Sparrow, "On Spectroscopic Resolving Power," *The Astrophysical Journal*, vol. 44, no. 76, p. 76, sep 1916. [Online]. Available: <http://adsabs.harvard.edu/doi/10.1086/142271>
36. E. Neuwirthová, Z. Lhotáková, and J. Albrechtová, "The Effect of Leaf Stacking on Leaf Reflectance and Vegetation Indices Measured by Contact Probe during the Season," *Sensors*, vol. 17, no. 6, p. 1202, may 2017. [Online]. Available: <http://www.mdpi.com/1424-8220/17/6/1202>
37. J. Kirz, "Phase zone plates for x rays and the extreme uv," *Journal of the Optical Society of America*, vol. 64, no. 3, p. 301, mar 1974. [Online]. Available: <https://www.osapublishing.org/abstract.cfm?URI=josa-64-3-301>
38. A. Lumsdaine, "Focused plenoptic camera and rendering," *Journal of Electronic Imaging*, vol. 19, no. 2, p. 021106, apr 2010. [Online]. Available: <http://electronicimaging.spiedigitallibrary.org/article.aspx?doi=10.1117/1.3442712>
39. C. D. Diaz, A. L. Franz, and M. A. Marciniak, "Frequency analysis and optimization of a spectral intermediate image diffractive plenoptic

camera,” in *Algorithms, Technologies, and Applications for Multispectral and Hyperspectral Imagery XXV*, D. W. Messinger and M. Velez-Reyes, Eds. SPIE, may 2019, p. 50. [Online]. Available: <https://www.spiedigitallibrary.org/conference-proceedings-of-spie/10986/2519036/Frequency-analysis-and-optimization-of-a-spectral-intermediate-image-diffractive/10.1117/12.2519036.full>

# REPORT DOCUMENTATION PAGE

Form Approved  
OMB No. 0704-0188

The public reporting burden for this collection of information is estimated to average 1 hour per response, including the time for reviewing instructions, searching existing data sources, gathering and maintaining the data needed, and completing and reviewing the collection of information. Send comments regarding this burden estimate or any other aspect of this collection of information, including suggestions for reducing this burden to Department of Defense, Washington Headquarters Services, Directorate for Information Operations and Reports (0704-0188), 1215 Jefferson Davis Highway, Suite 1204, Arlington, VA 22202-4302. Respondents should be aware that notwithstanding any other provision of law, no person shall be subject to any penalty for failing to comply with a collection of information if it does not display a currently valid OMB control number. PLEASE DO NOT RETURN YOUR FORM TO THE ABOVE ADDRESS.

<b>1. REPORT DATE (DD-MM-YYYY)</b> 24-02-2020		<b>2. REPORT TYPE</b> Master's Thesis		<b>3. DATES COVERED (From — To)</b> Jun 2019 — Mar 2020	
<b>4. TITLE AND SUBTITLE</b>  Multi-Spectral Imaging of Vegetation with a Diffractive Plenoptic Camera				<b>5a. CONTRACT NUMBER</b>	
				<b>5b. GRANT NUMBER</b>	
				<b>5c. PROGRAM ELEMENT NUMBER</b>	
				<b>5d. PROJECT NUMBER</b>	
<b>6. AUTHOR(S)</b>  Naranjo, Tristan R, 2d Lt				<b>5e. TASK NUMBER</b>	
				<b>5f. WORK UNIT NUMBER</b>	
				<b>8. PERFORMING ORGANIZATION REPORT NUMBER</b>  AFIT-ENP-MS-20-M-108	
<b>7. PERFORMING ORGANIZATION NAME(S) AND ADDRESS(ES)</b> Air Force Institute of Technology Graduate School of Engineering and Management (AFIT/EN) 2950 Hobson Way WPAFB OH 45433-7765				<b>9. SPONSORING / MONITORING AGENCY NAME(S) AND ADDRESS(ES)</b>  Undisclosed	
<b>10. SPONSOR/MONITOR'S ACRONYM(S)</b>				<b>11. SPONSOR/MONITOR'S REPORT NUMBER(S)</b>	
<b>12. DISTRIBUTION / AVAILABILITY STATEMENT</b> Distribution Statement A: Approved for Public Release; Distribution unlimited.					
<b>13. SUPPLEMENTARY NOTES</b> This work is declared a work of the U.S. Government and is not subject to copyright protection in the United States.					
<b>14. ABSTRACT</b> Snapshot multi-spectral sensors allow for object detection based on its spectrum for remote sensing applications. By making these sensors more light-weight, it allows for increased performance for drones and lower costs for satellites. To address this need, I designed and built a diffractive plenoptic camera (DPC) which utilized a Fresnel zone plate and a light field camera to detect vegetation via a normalized difference vegetation index (NDVI). This thesis aims to derive design equations of the DPC to get an estimate on its performance and evaluate the DPC's multi-spectral performance. The experimental results yielded that the spectral resolution near the design wavelength was 25 nm which exceed the estimated value of 6.06 nm. In capturing multi-spectral scenes, the DPC was able to identify vegetation in the scene at reduced values in comparison to a grating spectrometer. Additionally, artifacts unique to the DPC were found and discussed. The future of this work includes using a different diffractive optic design, using an intermediate image diffractive plenoptic camera, and using 3D deconvolution techniques.					
<b>15. SUBJECT TERMS</b> Computational imaging, plenoptic camera, light field camera, diffractive optics, Fresnel zone plate, Diffractive Plenoptic Camera, remote sensing, vegetation sensing, normalized difference vegetation index					
<b>16. SECURITY CLASSIFICATION OF:</b>			<b>17. LIMITATION OF ABSTRACT</b>	<b>18. NUMBER OF PAGES</b>	<b>19a. NAME OF RESPONSIBLE PERSON</b>
<b>a. REPORT</b>	<b>b. ABSTRACT</b>	<b>c. THIS PAGE</b>			Lt Col Anthony Franz, AFIT/ENP
U	U	U	UU	76	<b>19b. TELEPHONE NUMBER (include area code)</b> (937)255-3636 x4429    anthony.franz@us.af.mil

Standard Form 298 (Rev. 8-98)  
Prescribed by ANSI Std. Z39.18